

Investigating charge carrier scattering processes in anisotropic semiconductors through first-principles calculations: The case of p-type SnSe

Anderson S. Chaves,^{1,*} Robert Luis González-Romero,^{2,†} Juan J. Meléndez,^{3,‡} and Alex Antonelli^{4,§}

¹*Instituto de Física Gleb Wataghin, Universidade Estadual de Campinas, UNICAMP, 13083-859 Campinas, São Paulo, Brazil*

²*Departamento de Sistemas Físicos, Químicos y Naturales,*

Universidad Pablo de Olavide, Ctra. de Utrera, km. 1, 41013 Sevilla, Spain

³*Department of Physics, University of Extremadura, Avenida de Elvas, s/n, 06006 Badajoz, and Institute for Advanced Scientific Computing of Extremadura (ICCAEx), Avda. de Elvas, s/n, 06006 Badajoz, Spain*

⁴*Instituto de Física Gleb Wataghin and Centre for Computational Engineering & Sciences, Universidade Estadual de Campinas, UNICAMP, 13083-859 Campinas, São Paulo, Brazil*

(Dated: June 11, 2020)

Efficient *ab initio* computational methods for the calculation of thermoelectric transport properties of materials are of great avail for energy harvesting technologies. The **BoltzTraP** code has been largely used to efficiently calculate thermoelectric coefficients. However, its current version that is publicly available is based only on the constant relaxation time (RT) approximation, which usually does not hold for real materials. Here, we extended the implementation of the **BoltzTraP** code by incorporating realistic k-dependent RT models of the temperature dependence of the main scattering processes, namely, screened polar and nonpolar scattering by optical phonons, scattering by acoustic phonons, and scattering by ionized impurities with screening. Our RT models are based on a smooth Fourier interpolation of Kohn-Sham eigenvalues and its derivatives, taking into account non-parabolicity (beyond the parabolic or Kane models), degeneracy and multiplicity of the energy bands on the same footing, within very low computational cost. In order to test our methodology, we calculated the anisotropic thermoelectric transport properties of low temperature phase (*Pnma*) of intrinsic p-type and hole-doped tin selenide (SnSe). Our results are in quantitative agreement with experimental data, regarding the evolution of the anisotropic thermoelectric coefficients with both temperature and chemical potential. Hence, from this picture, we also obtained the evolution and understanding of the main scattering processes of the overall thermoelectric transport in p-type SnSe.

I. Introduction

Thermoelectric (TE) devices are heat engines based on an all-solid-state technology that attempt to harvest renewable energy from waste heat or function as heat pumps. Their properties make them suitable for several potential applications including automotive exhaust systems or solar energy converters [1]. However, their widespread commercial use has been hampered by their low efficiency, and hence, efforts towards the enhancement of TE conversion efficiency has been intensified in the last years. Highly efficient TE devices demand materials that exhibit high figures of merit (zT), a dimensionless quantity defined as $zT = (\sigma S^2 / \kappa) T$ (where S is the Seebeck coefficient, σ is the electrical conductivity, κ is the total thermal conductivity and T is an average temperature of operation), along with a large temperature gradient across the materials. Consequently, the optimization of zT is obtained by lowering κ while maintaining high the power factor ($PF = \sigma S^2$).

Several ways have been attempted in order to obtain

optimized zT values, including the reduction of κ through the enhancement of scattering processes for phonons by embedding nanostructures [2–5]. In addition, other strategies deal with the challenge of maximizing PF , which is strongly hampered by the conundrum that σ and S are inversely interdependent and hence, recent strategies, based on modifications in the band structure of existing semiconductors have been proposed, such as increasing band degeneracy within convergence of bands [3, 6] or taking advantage of their band structure anisotropy [7] and non-parabolicity [8].

In order to evaluate TE transport coefficients, the demand for more efficient computational approaches has increased. In particular, methods within the solution of Boltzmann transport equation (BTE) and the relaxation time approximation (RTA) have been extensively used, including transport models largely based on the dispersive effective mass, m_{eff} , as an adjustable parameter in closed-form expressions for the scattering mechanisms. Those models, such as single parabolic band (SPB) [9, 10] or Kane models, adjust m_{eff} to fit the calculated transport properties to the experimental data and often impressively capture transport properties over a range of temperatures and carrier concentrations. Meanwhile, the anisotropy can be captured by the use of anisotropic effective mass tensors. However, those models impose limitations in the understanding of TE properties and their improvement, since they are based on m_{eff} and not on the

*Electronic address: aschaves@ifi.unicamp.br

†Electronic address: robertl2703@gmail.com

‡Electronic address: melendez@unex.es

§Electronic address: aantone@ifi.unicamp.br

density of states effective mass, m^* . Even though within Kane models non-parabolicity can be taken into account, the consideration of multiplicity and degeneracy of band edges is not straightforward. For example, in the two-band Kane model, the interaction between valence band maximum (VBM) and conduction band minimum (CBM) is treated using the perturbative $\mathbf{k}\cdot\mathbf{p}$ method, while the remaining bands are neglected.

Other BTE-RTA based models relying directly on the *ab initio* bandstructure have led to a more realistic description of TE transport properties. Approximating the quasi-particle energies by Kohn-Sham (KS) eigenvalues, within density functional theory (DFT) framework [11, 12], it is usually possible to access band structure dependent quantities with relative simplicity from the analytical representation of the bands obtained from the interpolation schemes [13–17]. The **BoltzTraP** code [18] has been extensively adopted to this end [19–23], particularly due to its numerical stability and efficiency in interpolating band structure by using the smooth Fourier interpolation method and then solving the linearized BTE-RTA by performing all the required integrations. However, the current version of **BoltzTraP** that is publicly available is based only on the constant RTA, with resulting TE coefficients weighted by an unknown averaged relaxation time (RT), τ . This consideration ultimately takes τ to be direction independent, a feature that usually does not hold for real materials, which may possess strongly anisotropic Fermi-surface topology. Additionally, τ may possess a strong dependence with temperature and chemical potential that should be considered for real materials.

Ab initio models for the scattering mechanisms and their RTs certainly improve the understanding of transport properties and aid in the search for the next-generation of high-performing TE materials [24]. In this context, electron-phonon (*el-ph*) interactions have been fully treated within the *ab initio* framework, which enabled the calculation of mobility at different electron concentrations for several systems, for example, silicon [25–27], SrTiO₃ [28] and GaAs [29]. However, to the best of our knowledge, such approaches have been limited to few specific systems, which is mainly attributed to the high computational cost, even in the case of short ranged *el-ph* interactions of metals and nonpolar semiconductors. For polar semiconductors and oxides, the situation is even more challenging from this viewpoint, since the *ab initio* treatment of the long range Fröhlich interaction [30] involves a very large number of *e-ph* matrix elements to attain convergence. Recently, improvements regarding this problem have been achieved by splitting up the *e-ph* matrix elements into short- and long-range contributions [31, 32], in which the long-range part can be treated by using an analytical formula based on the Vogl model [33], while the short-range part is well-behaved. Very recently, a combination of the many-body theory of the electron-phonon interaction and the Boltzmann transport formalism, within an *ab initio* framework, was

used to obtain the temperature-induced renormalization of the electronic and transport problems of SnSe [34, 35]. However, the daunting task of calculating RTs over the entire Brillouin zone (BZ) is still extremely computationally demanding for three-dimensional systems.

In this paper, our aim is to implement realistic models for the RT within **BoltzTraP**, that go beyond parabolic or Kane models, in order to include non-parabolicity, multiplicity and degeneracy of the band edges on the same footing, however, at a much lower computational cost than that of fully *ab initio* approaches. In order to proceed, we considered \mathbf{k} -dependent RT models of the temperature dependence of the main scattering processes, namely, screened polar and nonpolar scattering by optical phonons, scattering by acoustic phonons, and scattering by ionized impurities with screening. Our implementation took advantage of the original **BoltzTraP** implementation concerning the calculations of band velocities within the RT formulae using the smooth Fourier interpolation of KS eigenvalues and its derivatives. As it will be discussed later, our methodology can explain many experimental transport data using in fact only very few fitting parameters, derived for only one temperature and chemical potential and subsequently extending it to larger ranges of temperature and carrier concentration.

In order to test our methodology, we calculated the anisotropic TE transport properties of the low temperature phase (*Pnma*) of p-type tin selenide (SnSe), which is one of the highest-performing TE materials known that has recently attracted much research interest [36–41]. The motivation for choosing this specific material comprises its intrinsic anisotropy along with non-parabolicity, degeneracy, and multiplicity of band edges, influencing TE transport properties. Hence, the understanding of their scattering mechanisms with temperature and chemical potential is of utmost importance in order to obtain hints about next-generation high-performing TE materials. Consequently, the subject of the present research is to report on the dominant anisotropic charge carrier scattering mechanisms in SnSe considering different temperature and carrier concentration ranges, in which experimental transport data have been used to probe the limits of our methodology.

II. Theoretical Approach

1. BTE within the RTA

Our methodology for carrier transport is based on the numerical solution to the semiclassical BTE, which has been applied to some extent to semiconductors. In the diffusive transport limit, in the presence of a temperature gradient (∇T) and applied electric (\mathbf{E}) and magnetic fields (\mathbf{B}), carrier transport properties can be obtained by solving the semiclassical BTE for the nonequilibrium

carrier distribution function $f_{n,\mathbf{k}} = f(\epsilon_{n,\mathbf{k}})$

$$\frac{\partial f_{n,\mathbf{k}}}{\partial t} + \mathbf{v}_{n,\mathbf{k}} \cdot \nabla_{\mathbf{r}} f_{n,\mathbf{k}} - \frac{\mathbf{F}}{\hbar} \cdot \nabla_{\mathbf{k}} f_{n,\mathbf{k}} = \left(\frac{\partial f_{n,\mathbf{k}}}{\partial t} \right)_{coll}, \quad (1)$$

where, n and \mathbf{k} label the band index and the wavevector, respectively. The electronic band velocity of the carrier in the $\{n, \mathbf{k}\}$ state with energy $\epsilon_{n,\mathbf{k}}$ is defined as $\mathbf{v}_{n,\mathbf{k}} = 1/\hbar \nabla_{\mathbf{k}} \epsilon_{n,\mathbf{k}}$, while the external force is given by $\mathbf{F} = e(\mathbf{E} + \mathbf{v}_{n,\mathbf{k}} \times \mathbf{B})$, where e is the absolute value of the charge carrier. The right-hand side term is related to charge carrier collisions and describes different sources of scattering and dissipation driving the system into a steady state. This scattering term can be expressed by introducing the per-unit-time probability, $W(n, \mathbf{k}|j, \mathbf{k}')$, of the transition of the charge carrier from the state $\{n, \mathbf{k}\}$ to state $\{j, \mathbf{k}'\}$, as a result of a particular scattering mechanism. From the principle of detailed equilibrium, the number of charge carriers coming into the state $\{j, \mathbf{k}'\}$ from $\{n, \mathbf{k}\}$ is the same as the number coming out from $\{j, \mathbf{k}'\}$ into $\{n, \mathbf{k}\}$, we have

$$\left(\frac{\partial f_{n,\mathbf{k}}}{\partial t} \right)_{coll} = \sum_{j,\mathbf{k}'} [W(j, \mathbf{k}'|n, \mathbf{k}) f_{j,\mathbf{k}'} (1 - f_{n,\mathbf{k}}) - W(n, \mathbf{k}|j, \mathbf{k}') f_{n,\mathbf{k}} (1 - f_{j,\mathbf{k}'})]. \quad (2)$$

The knowledge of $f_{n,\mathbf{k}}$ allows the evaluation of the charge current density

$$\mathbf{j} = -\frac{2e}{V} \sum_n \sum_{\mathbf{k}} \mathbf{v}_{n,\mathbf{k}} f_{n,\mathbf{k}} = -\frac{2e}{(2\pi)^3} \sum_n \int \mathbf{v}_{n,\mathbf{k}} f_{n,\mathbf{k}} d\mathbf{k}, \quad (3)$$

and the heat energy flux density

$$\mathbf{j}_Q = \frac{2}{V} \sum_n \sum_{\mathbf{k}} (\epsilon_{n,\mathbf{k}} - \mu) \mathbf{v}_{n,\mathbf{k}} f_{n,\mathbf{k}} = \frac{2}{(2\pi)^3} \sum_n \int (\epsilon_{n,\mathbf{k}} - \mu) \mathbf{v}_{n,\mathbf{k}} f_{n,\mathbf{k}} d\mathbf{k}, \quad (4)$$

where the factor 2 appears due to the electron spin, V is the crystal's volume, and μ is the chemical potential.

In order to proceed, we consider that the system is close enough to equilibrium so that the nonequilibrium distribution function, $f_{n,\mathbf{k}}$, differs only slightly from that of the equilibrium state, $f_{n,\mathbf{k}}^{(0)}$, that is $\Delta f(n, \mathbf{k}) = |f_{n,\mathbf{k}} - f_{n,\mathbf{k}}^{(0)}| \ll f_{n,\mathbf{k}}^{(0)}$. Within such approximation, Eq. (2) can be written in the RTA

$$\left(\frac{\partial f_{n,\mathbf{k}}}{\partial t} \right)_{coll} = -\frac{\Delta f(n, \mathbf{k})}{\tau_{n,\mathbf{k}}}, \quad (5)$$

where

$$\frac{1}{\tau_{n,\mathbf{k}}} = \sum_{\mathbf{k}'} \sum_j W(n, \mathbf{k}|j, \mathbf{k}') \left(\frac{1 - f_{j,\mathbf{k}'}^{(0)}}{1 - f_{n,\mathbf{k}}^{(0)}} - \frac{f_{n,\mathbf{k}}^{(0)}}{f_{j,\mathbf{k}'}^{(0)}} \frac{\Delta f(j, \mathbf{k}')}{\Delta f(n, \mathbf{k})} \right), \quad (6)$$

given the absence of quantization effects, thus $W(n, \mathbf{k}|j, \mathbf{k}')$ does not depend on \mathbf{E} , \mathbf{B} , or ∇T . Consequently, in the case of a homogeneous system, zero magnetic field, and a time-independent electric field, in the steady-state limit, Eq. (1) simplifies to

$$\mathbf{v}_{n,\mathbf{k}} \cdot \nabla_{\mathbf{r}} f_{n,\mathbf{k}} - \frac{e\mathbf{E}}{\hbar} \cdot \nabla_{\mathbf{k}} f_{n,\mathbf{k}} = -\frac{\Delta f(n, \mathbf{k})}{\tau_{n,\mathbf{k}}}, \quad (7)$$

from which it is possible to obtain the nonequilibrium distribution function provided that $\tau_{n,\mathbf{k}}$ does not depend on \mathbf{E} or ∇T .

Moreover, from the smallness of the deviation from equilibrium, $f_{n,\mathbf{k}}$ can be expanded to first order as

$$f_{n,\mathbf{k}} = f_{n,\mathbf{k}}^{(0)} - \tau_{n,\mathbf{k}} \mathbf{v}_{n,\mathbf{k}} \cdot \Phi_{\mathbf{0}}(\epsilon) \left(\frac{\partial f^{(0)}}{\partial \epsilon} \right), \quad (8)$$

where $\Phi_{\mathbf{0}}(\epsilon) = -e\mathcal{E} - \frac{\epsilon - \mu}{T} \nabla T$ is the generalized disturbing force (dynamic and static) causing the deviation from the equilibrium distribution, where $\mathcal{E} = \mathbf{E} + (1/e)\nabla\mu = -\nabla(\phi_0 - (\mu/e))$ is the gradient of the electrochemical potential. Substituting Eq. 8 into Eq. (6) we obtain

$$\frac{1}{\tau_{n,\mathbf{k}}} = \sum_{\mathbf{k}'} \sum_j W(n, \mathbf{k}|j, \mathbf{k}') \frac{1 - f^{(0)}(\epsilon')}{1 - f^{(0)}(\epsilon)} \left(1 - \frac{\tau_{j,\mathbf{k}'} \mathbf{v}_{j,\mathbf{k}'} \cdot \Phi_{\mathbf{0}}(\epsilon')}{\tau_{n,\mathbf{k}} \mathbf{v}_{n,\mathbf{k}} \cdot \Phi_{\mathbf{0}}(\epsilon)} \right). \quad (9)$$

Considering that the per-unit-time probability of charge carrier transition, $W(n, \mathbf{k}|j, \mathbf{k}')$, does not depend on \mathbf{k} and \mathbf{k}' separately, but only on the magnitudes of the vectors, $|\mathbf{k}|$ and $|\mathbf{k}'|$, and the angle between them, $\mathbf{k} \cdot \mathbf{k}'$, that is $W(n, \mathbf{k}|j, \mathbf{k}') = W_{n,j}(|\mathbf{k}|, |\mathbf{k}'|, \mathbf{k} \cdot \mathbf{k}')$. Additionally, considering that the dispersion relation is an arbitrary spherically symmetric function of the magnitude of the wavevector, $k = |\mathbf{k}|$, (not necessarily parabolic) and the charge carrier scattering is purely elastic, that is, the charge carriers exchange energy during scattering only by impulses with $\epsilon(|\mathbf{k}|) = \epsilon(|\mathbf{k}'|)$, Eq. (9) may be rewritten as [42]

$$\frac{1}{\tau_{n,k}} = \sum_{\mathbf{k}'} \sum_j W(n, \mathbf{k}|j, \mathbf{k}') \left(1 - \frac{\mathbf{k} \cdot \mathbf{k}'}{k^2} \right). \quad (10)$$

At this point, some comments are in order. Although Eq. (10) has been derived for isotropic bands, results obtained from it have been used to study transport properties of lead chalcogenides, which are anisotropic [43, 44].

The use of this methodology in this case is possible because, although anisotropic, the transport properties in these materials along the different directions are mutually independent, except for the magnetoresistance, which essentially depends on the anisotropy. As it will be clear later, the application of this methodology in the case of SnSe is justified by the good agreement of our results with the experiment at different values of temperature and chemical potential.

2. TE Kinetic Coefficients Tensors

The tensorial formalism is appropriate to discuss TE effects for anisotropic materials. The off-diagonal coupling between the electronic current density, \mathbf{j} , and heat energy flux density, \mathbf{j}_Q , can be derived on a more general basis within the linear response theory [45] as

$$\begin{bmatrix} \mathbf{j} \\ \mathbf{j}_Q \end{bmatrix} = \begin{bmatrix} \mathbf{L}^{11} & \mathbf{L}^{12} \\ \mathbf{L}^{21} & \mathbf{L}^{22} \end{bmatrix} \cdot \begin{bmatrix} \boldsymbol{\varepsilon} \\ -\frac{\nabla T}{T} \end{bmatrix} \quad (11)$$

in which, \mathbf{L}^{11} , \mathbf{L}^{12} , \mathbf{L}^{21} , \mathbf{L}^{22} are the moments of the generalized transport coefficients, which we will call kinetic coefficient tensors, with $\mathbf{L}^{12} = \mathbf{L}^{21}$ based on the Onsager reciprocity relations [45]. Such kinetic coefficients can be expressed as

$$\Lambda^{(\alpha)}(\mu; T) = e^2 \int \Xi(\epsilon, \mu, T) (\epsilon - \mu)^\alpha \left(-\frac{\partial f^{(0)}(\mu; \epsilon, T)}{\partial \epsilon} \right) d\epsilon, \quad (12)$$

with $\mathbf{L}^{11} = \Lambda^{(0)}$, $\mathbf{L}^{21} = \mathbf{L}^{12} = -(1/e)\Lambda^{(1)}$, and $\mathbf{L}^{22} = (1/e^2)\Lambda^{(2)}$, in which $\Xi(\epsilon, \mu, T)$ is the transport distribution kernel (TDK) given by

$$\Xi(\epsilon, \mu, T) = \int \sum_n \mathbf{v}_{n,\mathbf{k}} \otimes \mathbf{v}_{n,\mathbf{k}} \tau_{n,\mathbf{k}}(\mu, T) \delta(\epsilon - \epsilon_{n,\mathbf{k}}) \frac{d\mathbf{k}}{8\pi^3}. \quad (13)$$

At both experimental conditions of zero temperature gradient ($\nabla T = 0$) and zero electric current, the kinetic coefficient tensors can be identified with the electrical conductivity tensor, $\sigma = \Lambda^{(0)}$, with the Seebeck coefficient tensor, $S = (eT)^{-1}\Lambda^{(1)}/\Lambda^{(0)}$, and with the charge carrier contribution to the thermal conductivity tensor, $\kappa_{elec} = (e^2T)^{-1}(\Lambda^{(1)} \cdot \Lambda^{(0)^{-1}} \cdot \Lambda^{(1)} - \Lambda^{(2)})$.

A. Scattering Mechanisms and the RTA

Within the Born approximation in the scattering theory, the magnitude of the Hamiltonian of the charge carrier interaction, H' , is considered to deviate only slightly from the magnitude of the non-perturbed Hamiltonian, H , that is, $H' - H \ll H$. The transition probability per-unit-time between Bloch states $\Psi_{j,\mathbf{k}'}$ and $\Psi_{n,\mathbf{k}}$ can be obtained from the first order perturbation theory

(Fermi's golden rule)

$$W(n, \mathbf{k}|j, \mathbf{k}') = \frac{2\pi}{\hbar} |\langle \Psi_{j,\mathbf{k}'} | H' | \Psi_{n,\mathbf{k}} \rangle|^2 \delta(\epsilon_{j,\mathbf{k}'} - \epsilon_{n,\mathbf{k}}), \quad (14)$$

which is valid in the so-called weak coupling regime [46]. Integrating out such probability over the BZ, the total scattering rate is obtained. Specifically, in the presence of a phonon field, an electron in the Bloch state $\Psi_{n,\mathbf{k}}$ will experience a perturbation H' , inducing a transition to the state $\Psi_{j,\mathbf{k}'}$. In such a process, momentum and energy are conserved so that $\mathbf{k}' = \mathbf{k} \pm \mathbf{q}$ and $\epsilon_{j,\mathbf{k}'} = \epsilon_{n,\mathbf{k}} \pm \hbar\omega_{\mathbf{q}}^\lambda$, where $\omega_{\mathbf{q}}^\lambda$ is the phonon frequency with wave vector \mathbf{q} and mode number λ . The plus-minus sign refers to phonon absorption or emission, respectively. The respective per-unit-time transition probability is calculated from Eq. (14) as

$$W(n, \mathbf{k}|j, \mathbf{k} \pm \mathbf{q}) = \frac{2\pi}{\hbar} |\langle \Psi_{j,\mathbf{k} \pm \mathbf{q}} | H'^\lambda | \Psi_{n,\mathbf{k}} \rangle|^2 \delta(\epsilon_{j,\mathbf{k} \pm \mathbf{q}} - \epsilon_{n,\mathbf{k}} \mp \hbar\omega_{\mathbf{q}}^\lambda). \quad (15)$$

By using the above equations along with equation (10), expressions for the different scattering mechanisms RTs can be derived, mostly following Ref. [42], as will be discussed below.

1. Carrier-Acoustic Phonons Non-polar Scattering

The deformation potential technique, as introduced by Bardeen and Shockley [47] and extended by Herring and Vogt [48] has been used to derive an expression for the RT for the non-polar scattering of charge carrier by acoustic phonons. When an acoustic wave with vanishing \mathbf{q} vector travels through a finite crystal it may induce shifts in the spacing between neighboring atoms, resulting in local fluctuations of the energy band gap. These are known as acoustic deformation potentials (ADPs), which can be measured by quantifying the energy variation of the valence and conduction band edges per unit of strain. The former variation represents the interaction energy of holes with lattice oscillations. The magnitude of the shifts, \mathbf{u}_s , are given in terms of plane waves as

$$\mathbf{u}_s(\mathbf{r}) = \frac{1}{\sqrt{N}} \sum_{\mathbf{q}} \sum_{\lambda=1}^3 \mathbf{e}_\lambda(\mathbf{q}) \cdot [b_{\lambda,\mathbf{q}} \exp(i\mathbf{q} \cdot \mathbf{r}) + b_{\lambda,\mathbf{q}}^* \exp(-i\mathbf{q} \cdot \mathbf{r})], \quad (16)$$

where \mathbf{r} are the atomic coordinates in real space, N is the number of atoms in the periodic crystal, $\mathbf{e}_\lambda(\mathbf{q})$ is the polarization unit vector and $b_{\lambda,\mathbf{q}}$ are the complex normal coordinates. In Eq. (16), all atoms in the elementary unit cell oscillate in phase and the interaction energy must be proportional to the first derivative of the $\mathbf{u}_s(\mathbf{r})$ with respect to \mathbf{r}

$$H'_{ac} = E_1 \nabla \mathbf{u}_s(\mathbf{r}), \quad (17)$$

where E_1 is the effective deformation potential.

Going back to Eq. (14), it is possible to obtain the per-unit-time transition probability, and, along with Eq. (10), the RT for a given electronic band n can be written as

$$\frac{1}{\tau_{\mathbf{k}}} = \frac{2\pi}{MN} \frac{E_1^2}{\hbar v_0^2} k_B T \sum_{\mathbf{k}'} \left(1 - \frac{\mathbf{k} \cdot \mathbf{k}'}{kk'}\right) \delta(\epsilon_{\mathbf{k}'} - \epsilon_{\mathbf{k}}), \quad (18)$$

where M is the atomic mass and v_0 is the sound velocity. In Eq. (18), it was considered that the scattering is elastic, and hence, the phonon energy has been neglected. Such approximation, is valid for $T \gg 1\text{K}$ [42], which meets the conditions usually found in TE applications. Finally, considering that the electronic dispersion is arbitrary but spherically symmetric, the summation over \mathbf{k}' can be turned into an integral that can be solved by using spherical coordinates and properties of δ -functions. Hence, one finds the following expression for the RT for non-polar scattering of charge carriers by acoustic phonons in a single band n

$$\tau_{ac}(k) = \frac{\pi \hbar \rho}{E_1^2} \frac{v_0^2}{k_B T} \frac{1}{k^2} \left| \frac{\partial \epsilon_k}{\partial k} \right|, \quad (19)$$

where, $\rho = MN/V$ is the mass density of the material and V is the crystal volume.

2. Carrier-Optical Phonons Non-polar Scattering

In more complex crystal lattices with two or more atoms in the unit cell, alongside with the scattering by acoustic phonons, the polar and non-polar scattering by optical phonons are at play. The idea of deformation potentials has been extended to the interaction between charge carriers and long-wavelength ($\mathbf{q} \rightarrow 0$) non-polar optical phonons, giving rise to the optical deformation potentials (ODP), corresponding to shifts of the electronic bands due to relative displacement between two sublattices of the crystal. Unlike the scattering by acoustic lattice oscillations, optical phonons oscillate out of phase, and the center of mass remains at rest. In the case of the scattering by non-polar optical phonons, the interaction energy related to the induced variation of the energy band gap should be proportional to the shift of any atom in the unit cell [42]

$$H'_{npol} = \sum_{\lambda=4}^{3s} \mathbf{A}_{\lambda} \mathbf{u}_{\mathbf{s}}^{\lambda}, \quad (20)$$

where \mathbf{A}_{λ} is a constant vector related to the symmetry of the arrangement of the band edges, $\mathbf{u}_{\mathbf{s}}^{\lambda}$ is the atomic displacement (similar to Eq. (16)) associated with mode λ , and s is the number of atoms in the unit cell. Consequently, the energy operator in this case appears to be much more involving than the case of acoustic phonons. In order to proceed, an effective vector can be taken to represent all interactions in an average manner, and

hence, all the complexity can be encompassed within such effective vector. Considering a specific optical phonon branch, λ , in which the scattering is occurring on its minimum, \mathbf{A} can be defined as

$$\mathbf{A} = E_0 \mathbf{b}_g, \quad (21)$$

where E_0 is the effective ODP, $\mathbf{b}_g = (\pi/a)\mathbf{g}$ is the reciprocal lattice vector with \mathbf{g} being a unit vector directed from the BZ center to the minimum, while a is the lattice constant.

Within the previous considerations, the per-unit-time transition probability for charge carriers, for a specific band n , can be obtained as

$$W_{npol}(\mathbf{k}|\mathbf{k}') = \frac{\pi E_0^2}{NM\omega_0} \left(\frac{\pi}{a}\right)^2 [N_0 \delta(\epsilon_{k'} - \epsilon_k - \hbar\omega_{\mathbf{q}}) + (N_0 + 1) \delta(\epsilon_{k'} - \epsilon_k + \hbar\omega_{\mathbf{q}})], \quad (22)$$

with $\omega_0 = \omega_{(\mathbf{q} \rightarrow 0)}$ and N_0 is the Bose-Einstein distribution. Additionally, we considered only coupling parallel to the unit polarization vector ($\mathbf{e}_{\lambda}(\mathbf{q})$). The non-polar scattering of charge carriers by optical phonons is essentially non-elastic, due to the magnitude of optical phonon energy. However, the description of this scattering within the RT approximation may arise from the evenness of the transition probability function, $W(\mathbf{k}|\mathbf{k}') = W(|\mathbf{k} - \mathbf{k}'|)$, which is a condition satisfied by the scattering probability as given by Eq. (22). On the basis of such considerations, at high temperatures, $k_B T \gg \hbar\omega_0$, the following simple expression is obtained for the RT for the non-polar scattering by optical phonons at a specified band n [42]

$$\tau_{npol}(k) = \frac{1}{\pi \hbar} \beta^2 \frac{\rho a^2}{k_B T} \frac{1}{k^2} \left| \frac{\partial \epsilon_k}{\partial k} \right|, \quad (23)$$

in which $\beta = \hbar\omega_0/E_0$ is the reciprocal ODP normalized by the energy of optical phonons. In particular, $\tau_{npol}(k)$ presents the same temperature dependence as the scattering by acoustic phonons.

3. Carrier-Optical Phonons Polar Scattering

In semiconductor compounds with some degree of ionic bonding, there is an additional interaction with charge carriers known as polar mode scattering, in which the charge carriers are scattered by the electric polarization caused by longitudinal optical (LO) phonons. This was firstly discussed by Fröhlich [49] and Callen [50], while Howarth and Sondheimer [51] developed the theory of polar mode scattering, on the basis of electrons as charge carriers on a simple parabolic conduction band. Following the derivation by Fröhlich [52], the electric polariza-

tion due to ion displacement is given by

$$\mathbf{P}(\mathbf{r}) = \left(\frac{\hbar\omega^{LO}(q)}{8\pi V\zeta^*} \right)^{1/2} \sum_{\mathbf{q}} \sum_{\lambda=4}^{3s} \mathbf{e}_\lambda \cdot [b_\lambda(\mathbf{q}) \exp(i\mathbf{q} \cdot \mathbf{r}) + b_\lambda^*(\mathbf{q}) \exp(-i\mathbf{q} \cdot \mathbf{r})], \quad (24)$$

where $\omega^{LO}(q)$ is the frequency of the LO phonons; $1/\zeta^* = 1/\zeta_\infty - 1/\zeta_0$, with ζ_∞ and ζ_0 being the high-frequency and the static dielectric constants, respectively. From the Poisson's equation we can derive the scalar potential of the polarization vector, $\nabla^2\phi = 4\pi\nabla \cdot \mathbf{P}(\mathbf{r})$, which yields the following interaction energy of the polar mode scattering of charge carriers by optical phonons

$$H'_{pol} = \pm e\phi = \mp ie \left(\frac{4\pi\hbar\omega^{LO}(q)}{2V\zeta^*} \right)^{1/2} \sum_{\mathbf{q}} \sum_{\lambda=4}^{3s} \frac{1}{q^2} (\mathbf{e}_\lambda \cdot \mathbf{q}) [b_\lambda(\mathbf{q}) \exp(i\mathbf{q} \cdot \mathbf{r}) + b_\lambda^*(\mathbf{q}) \exp(-i\mathbf{q} \cdot \mathbf{r})], \quad (25)$$

with $\mathbf{e}_\lambda \cdot \mathbf{q} = q$ in the case of LO phonons.

If the phonon dispersion is not considered, $\omega^{LO}(q) = \omega_0^{LO}$, then the following expression for the transition probability, at a specific band n , is obtained

$$W_{pol}(\mathbf{k}|\mathbf{k}') = \frac{4\pi^2 e^2}{V\zeta^*} \frac{\omega_0^{LO}}{(\mathbf{k}' - \mathbf{k})^2} \times [N_0\delta(\epsilon_{\mathbf{k}'} - \epsilon_{\mathbf{k}} + \hbar\omega_0^{LO}) + (N_0 + 1)\delta(\epsilon_{\mathbf{k}'} - \epsilon_{\mathbf{k}} - \hbar\omega_0^{LO})]. \quad (26)$$

Unlike non-polar mode scattering, from Eq. (26) it can be seen that $W_{pol}(\mathbf{k}|\mathbf{k}')$ is dependent on the directions \mathbf{k} and \mathbf{k}' and, generally, it is impossible to introduce RT for polar mode scattering of optical phonons. However, at high temperatures, $k_B T \gg \hbar\omega_0^{LO}$, the non-elasticity can be neglected with $\epsilon_{\mathbf{k}'} \sim \epsilon_{\mathbf{k}}$ and $N_0 + 1 \sim N_0 \sim k_B T / \hbar\omega_0^{LO}$, which yields

$$W_{pol}(\mathbf{k}|\mathbf{k}') = \frac{8\pi^2 e^2}{V\zeta^*} \frac{k_B T}{\hbar} \frac{1}{(\mathbf{k}' - \mathbf{k})^2} \delta(\epsilon_{\mathbf{k}'} - \epsilon_{\mathbf{k}}). \quad (27)$$

Thus, substituting Eq. 27 into Eq. (10) and transforming the summation over \mathbf{k}' into an integral that can be solved by using spherical coordinates and properties of δ -functions, it results in the following closed expression for the RT of polar mode scattering of optical phonons, given a specific band n ,

$$\tau_{pol}(k) = \frac{\zeta^* \hbar}{2e^2 k_B T} \left| \frac{\partial \epsilon_k}{\partial k} \right|, \quad (28)$$

which does not depend on the phonon-frequency in the high temperature limit.

The generalization to include screening effects was subsequently developed by Ehrenreich [53]. Free carriers that are present in the sample screen out the electric field produced by optical vibrations, resulting twofold ef-

fects in the quasi-static approximation, namely, a change in the matrix element of charge carrier interaction with optical phonons and a shift in the frequency of longitudinal optical mode [53]. The former effect decreases the transition probability by a factor of $1 - (r_0 q)^{-2}$, in which r_0 is the screening radius given by

$$r_0^{-2}(k) = \frac{4\pi e^2}{\zeta_0} \int -\frac{\partial f^{(0)}(\epsilon)}{\partial \epsilon_k} g(\epsilon) d\epsilon, \quad (29)$$

where $f^{(0)}(\epsilon)$ is the equilibrium electron distribution function and $g(\epsilon)$ is the density of states (DOS), which is given explicitly in Eq. (50). The latter effect leads to a frequency shift of the LO vibrations given by

$$(\omega^{LO})^2 = (\omega^{TO})^2 \left(\frac{\zeta_0/\zeta_\infty + (r_0 q)^{-2}}{1 + (r_0 q)^{-2}} \right), \quad (30)$$

where ω^{TO} is the transverse optical (TO) mode frequency. Therefore, the frequency of the LO phonon is strongly reduced, which also affects the transition probability [44]. The dynamical features of the screening were neglected here, since their effect is regarded to be quite small [44]. Hence, the consideration of quasi-static screening results in the following factor in the denominator of expression for the RT

$$F_{pol} = \left[1 - \frac{1}{2(r_0 k)^2} \ln[1 + 4(r_0 k)^2] + \frac{1}{1 + 4(r_0 k)^2} \right]^{-1}. \quad (31)$$

It is important to note that the energy dependence of RT is also changed because of the energy dependence of the screening through r_0 [44].

The necessary modifications when dealing with polar mode scattering of p-like symmetry holes have also been addressed [54–57], beyond the polar mode scattering of s-like electrons. The work by Wiley [57] gave the first quantitative discussion of overlap effects on the polar mobility of holes, showing that, for carriers with p-like valence bands, the mobility is about twice the mobility for carriers with pure s-like wave functions. Conclusions, in the same line of reasoning, that the mobility increases due to the p-like symmetry of wave functions, were obtained by Kranzer [54] on the basis of a numerical solution of the BTE and by Costato *et al.* [55] by using a Monte Carlo technique for solving the coupled BTE. Consequently, besides screening effects, it is also necessary to include the correction factor, K_{pol} , in the RT given by Eq. (47), due to the p-like symmetry of the wave functions, which is important, for example, in the case of polar mode scattering of holes. The way the correction factor K_{pol} is determined in the actual calculations will be discussed later in the article.

4. Carrier-Impurity Scattering

The consideration of extrinsic collision processes, beyond those involving the crystalline lattice, i.e., the intrinsic scattering by phonons, requires the presence of impurities in the crystal. Particularly, we will consider only the concentration of ionized impurities because the number of charged donors or acceptors is usually considerably larger than that of neutral imperfections. Ionized impurity scattering has been treated theoretically by Brooks and Herring (B-H) [58, 59], by considering a screened Coulomb potential, the Born approximation for the evaluation of transition probabilities, and neglecting the perturbation effects of the impurities on the electron energy levels and wave functions. In the B-H theory, the electron is scattered independently by dilute concentrations of ionized centers randomly distributed in semiconductors. It constitutes a good description without considering more complex effects, such as the contributions from coherent scattering from pairs of impurity centers, which requires a quantum transport theory [60].

The per-unit-time transition probability for the scattering of charge carriers by ionized impurities can be written in the plane-wave approximation as

$$W(\mathbf{k}|\mathbf{k}') = \frac{2\pi N_i}{\hbar V} \left| \int U(\mathbf{r}) \exp[i(\mathbf{k} - \mathbf{k}') \cdot \mathbf{r}] d\mathbf{r} \right|^2 \delta(\epsilon_{\mathbf{k}'} - \epsilon_{\mathbf{k}}), \quad (32)$$

where $U(\mathbf{r})$ is the scattering potential and N_i is the ionized impurity concentration.

The long-range Coulomb field, $U(r) = e\phi(r) = \pm e^2/\zeta_0 r$, where the potential ϕ at a point r of the crystal is due to the presence of positive (donor) or negative (acceptor) impurity ions. The straightforward application of this field in Eq. (32) leads to a logarithmic divergence, and hence, a screened Coulomb potential has to be considered. According to the B-H theory, the potential can be expressed in a more rigorous form as $\phi(r) = \pm e/\zeta_0 r (\exp(-r/r_0))$, where r_0 is the radius of ion field screening defined by Eq. (29). From Eqs. (10), (14), and (32), the RT for the scattering of charge carriers by ionized impurities can be expressed for each band n as

$$\tau_{imp}(k) = \frac{\hbar\zeta_0^2}{2\pi e^4 N_i F_{imp}(k)} k^2 \left| \frac{\partial \epsilon_k}{\partial k} \right| \quad (33)$$

where

$$F_{imp}(k) = \ln(1 + \eta) - \frac{\eta}{1 + \eta}, \quad (34)$$

is the screening function, with $\eta = (2kr_0)^2$.

III. Computational Implementation

The evaluation of carrier transport properties were carried out using the **BoltzTraP** code as a reference [18]. The **BoltzTraP** code solves the linearized BTE by Fourier interpolating the band structure computed within the DFT framework and performs all the integrations required to determine the TE transport properties.

1. Fourier Interpolation

In order to introduce the main ideas behind Fourier interpolation within **BoltzTraP**, let us consider N_{KS} KS eigenvalues for a given band n of a three-dimensional (3D) periodic solid. The symmetry of the crystal's reciprocal space is incorporated in the energy bands. Therefore, it is natural to use star functions, $\Upsilon_m(\mathbf{k})$, as basis set to Fourier expand the quasi-particles energies

$$\tilde{\epsilon}_{\mathbf{k}} = \sum_{m=1}^M a_m \Upsilon_m(\mathbf{k}), \quad (35)$$

where

$$\Upsilon_m(\mathbf{k}) = \frac{1}{n_s} \sum_{\{v\}} \exp[i(v\mathbf{R}_m) \cdot \mathbf{k}], \quad (36)$$

with the sum running over all n_s point group operations $\{v\}$ on the direct lattice translations, \mathbf{R}_m . The first derivatives are straightforwardly given by

$$\mathbf{v}_{\mathbf{k}} = \frac{\partial \tilde{\epsilon}_{\mathbf{k}}}{\partial \mathbf{k}} = \frac{i}{n_s} \sum_{m=1}^M a_m \sum_{\{v\}} (v\mathbf{R}_m) \exp[i(v\mathbf{R}_m) \cdot \mathbf{k}], \quad (37)$$

in which the main problem is the determination of Fourier coefficients, a_m .

BoltzTraP relies on the proposal by Shankland [61], according to which one should choose a set of basis functions for interpolation larger than the number of data points ($M > N_{KS}$) and constrain the interpolation function to pass exactly through such points. In order to obtain a smooth interpolation, the extra basis functions are used to minimize a roughness function suitably defined by Pickett, Krakauer and Allen [15]

$$\mathfrak{R} = \sum_{m=2}^M |a_m|^2 \rho(R_m) \quad (38)$$

with

$$\rho(R_m) = \left(1 - c_1 \left(\frac{R_m}{R_{min}} \right)^2 \right)^2 + c_2 \left(\frac{R_m}{R_{min}} \right)^6, \quad (39)$$

where $R_m = |\mathbf{R}_m|$, R_{min} is the magnitude of the smallest nonzero lattice vector, and $c_1 = c_2 = 3/4$. Thus, the

Lagrange multiplier method can now be used since the formulated problem is to minimize \mathfrak{R} subject to the constraints, $\tilde{\epsilon}_{\mathbf{k}_l} = \epsilon_{\mathbf{k}_l}$, with respect to the Fourier coefficients. From such minimization one obtains

$$a_m = \begin{cases} \rho(R_m)^{-1} \sum_{l=1}^{N_{KS}-1} \lambda_l^* [\Upsilon_m^*(\mathbf{k}_l) - \Upsilon_m^*(\mathbf{k}_{N_{KS}})], & m > 1 \\ \epsilon_{\mathbf{k}_{N_{KS}}} - \sum_{m=2}^M a_m \Upsilon_m(\mathbf{k}_{N_{KS}}), & m = 1 \end{cases} \quad (40)$$

in which the Lagrange multipliers, λ_l^* , can be evaluated from

$$\epsilon_{\mathbf{k}_p} - \epsilon_{\mathbf{k}_{N_{KS}}} = \sum_{l=1}^{N_{KS}-1} \mathbf{H}_{pl} \lambda_l^*, \quad (41)$$

with

$$\mathbf{H}_{pl} = \sum_{m=2}^M \frac{[\Upsilon_m(\mathbf{k}_p) - \Upsilon_m(\mathbf{k}_{N_{KS}})] [\Upsilon_m^*(\mathbf{k}_l) - \Upsilon_m^*(\mathbf{k}_{N_{KS}})]}{\rho(R_m)}. \quad (42)$$

2. Anisotropic \mathbf{k} -mesh

In practice, a finer and anisotropic \mathbf{k} -mesh can be generated for the interpolation. To accomplish this, lattice points and their respective star functions are generated in real space following point the group operations of the crystal symmetry. The corresponding translation vector can be given as $\mathbf{R} = u_1 \mathbf{a}_1 + u_2 \mathbf{a}_2 + u_3 \mathbf{a}_3$, in which $\mathbf{a}_1, \mathbf{a}_2, \mathbf{a}_3$ are related to the crystal primitive vectors. Such points are generated inside a sphere of a radius $R' = \sqrt[3]{3 \cdot n_{kpt} \cdot (M/N_{KS}) \cdot \Omega / 4\pi}$, where n_{kpt} is the number of \mathbf{k} -points of the original \mathbf{k} -mesh in the entire BZ, (M/N_{KS}) is the required number of star functions per \mathbf{k} -point and Ω is the volume of the unit cell. Consequently, R' determines the full extension of the real space and can be properly changed, for example, by increasing the number of star functions per \mathbf{k} -point. The corresponding reciprocal lattice, with a translation vector, $\mathbf{k} = k_1 \mathbf{b}_1 + k_2 \mathbf{b}_2 + k_3 \mathbf{b}_3$ can be determined by generating its three primitive vectors from the direct ones from $[\mathbf{b}_1 \mathbf{b}_2 \mathbf{b}_3]^T = [\mathbf{a}_1 \mathbf{a}_2 \mathbf{a}_3]^{-1}$, in which the 2π factor was omitted following the crystallographic definition of reciprocal space. In order to capture the crystal anisotropy, the extension of the real space can be determined for each crystal direction, defining spheres for each crystallographic axis with the maximum radius given by $R_{max}(t) = INT(R' \cdot \sqrt{\mathbf{b}_t \cdot \mathbf{b}_t}) + 1$, with $t = \{1, 2, 3\}$ and $INT(x)$ gives the largest integer number that does not exceed the magnitude of x . Hence, lattice points fill all the spheres space inside the $\{-R_{max}(t), R_{max}(t)\}$ range. Within **BoltzTraP**, a 3D array containing all vectors are sorted considering their concentric radius, r , from the sphere center, and providing that all vectors, \mathbf{R} , have different star functions, m . In practice, to determine all \mathbf{k} vectors from \mathbf{R}_m , a 3D Fast Fourier Transform (FFT) is performed, being possible to redefine a finer

and anisotropic \mathbf{k} -mesh.

The magnitude of each \mathbf{R}_m vector, r , is defined through the metric tensor formalism. Let us consider the scalar product of two arbitrary vectors in the coordinate system of the real space, $\mathbf{r}_1 \cdot \mathbf{r}_2 = (x_1 \mathbf{a}_1 + y_1 \mathbf{a}_2 + z_1 \mathbf{a}_3) \cdot (x_2 \mathbf{a}_1 + y_2 \mathbf{a}_2 + z_2 \mathbf{a}_3)$. In the matrix notation this is written as

$$\mathbf{r}_1 \cdot \mathbf{r}_2 = \begin{bmatrix} x_1 & y_1 & z_1 \end{bmatrix} \begin{bmatrix} \mathbf{a}_1 \cdot \mathbf{a}_1 & \mathbf{a}_1 \cdot \mathbf{a}_2 & \mathbf{a}_1 \cdot \mathbf{a}_3 \\ \mathbf{a}_2 \cdot \mathbf{a}_1 & \mathbf{a}_2 \cdot \mathbf{a}_2 & \mathbf{a}_2 \cdot \mathbf{a}_3 \\ \mathbf{a}_3 \cdot \mathbf{a}_1 & \mathbf{a}_3 \cdot \mathbf{a}_2 & \mathbf{a}_3 \cdot \mathbf{a}_3 \end{bmatrix} \begin{bmatrix} x_2 \\ y_2 \\ z_2 \end{bmatrix} = \bar{\mathbf{X}}_1 \mathbf{G} \mathbf{X}_2. \quad (43)$$

Considering that $\mathbf{r}_1 = \mathbf{r}_2 = \mathbf{R}_m$, the magnitude of the real space vector is given by $r = \sqrt{\bar{\mathbf{X}} \mathbf{G} \mathbf{X}}$, with $\bar{\mathbf{X}} = [u_1 u_2 u_3]$. For all \mathbf{R}_m in the Bravais lattice, the reciprocal lattice is characterized by a set of wavevectors \mathbf{k} , such that, $e^{2\pi i \mathbf{k} \cdot \mathbf{R}_m} = 1$. Given \mathbf{R}_m and \mathbf{k} in the same direction, the magnitude of the vector \mathbf{k} in the reciprocal space is given by $|\mathbf{k}| = (k_1 u_1 + k_2 u_2 + k_3 u_3) / r = n_{int}(1) + n_{int}(2) + n_{int}(3) / r$, where $n_{int}(t) = 1, 2, \dots, k_{max}(t)$ are integer numbers with $k_{max}(t) = 2R_{max}(t) + 1$ defining the \mathbf{k} -mesh grid. In practice, $k_{max}(t)$ should be carefully taken as the product of small primes in order to improve the efficiency of FFT. If we consider just one specific crystallographic axis, the magnitude of the \mathbf{k} vector can be determined for each axis by $|\mathbf{k}|_t = k_t = n_{int}(t) / r$. Hence, through the definition of anisotropic \mathbf{k} -mesh the anisotropy of materials TE properties can be captured.

3. Anisotropic RTs

The consideration of anisotropy in the RTs of the aforementioned scattering processes can now be introduced. We start by generalizing the closed expressions for all RTs formulae, comprising Eqs. (19), (23), (28), (33), for every band n by considering the interpolated quasi-particles energies, $\tilde{\epsilon}_{n,\mathbf{k}}$, and their derivatives. In such expressions for the RT, the explicit dependence on \mathbf{k} can have an arbitrary form, beyond the parabolic dependence. Hence, we may properly account for the multiplicity, degeneracy and non-parabolicity of the band edges on the same footing, along with anisotropy. The expression for the RT of the non-polar scattering by acoustic phonons can now be expressed along the direction t and for a given band index n

$$(\tau_{ac})_t(n, k) = \frac{\pi \hbar \rho}{(E_1)_t^2} \frac{(v_0)_t^2}{k_B T} \frac{1}{k_t^2} \left| \frac{\partial \epsilon_{n,k}}{\partial k_t} \right|, \quad (44)$$

in which the parameters have to be taken along each crystallographic axis, i.e., it is necessary to consider anisotropic parameters. Hence, the subscript t in Eq.(44), as well in the subsequent equations, indicates a given crystallographic direction. The acoustic deformation potential for holes and electrons can be calculated from *ab initio* methods on the basis of the energy change of the

VBM and CBM, respectively, with respect to a deep core state that is practically insensitive to slight lattice deformations. The anisotropic velocity entering in Eq.(44) as well as in the subsequent equations is defined as

$$v_t(n, \mathbf{k}) = \left(\frac{\partial \epsilon_{n, \mathbf{k}}}{\partial \mathbf{k}} \right)_t \approx \left(\frac{\partial \tilde{\epsilon}_{n, \mathbf{k}}}{\partial \mathbf{k}} \right)_t = \frac{i}{n_s} \sum_{m=1}^M a_m \sum_{\{v\}} (v \mathbf{R}_m)_t \exp[i(v \mathbf{R}_m) \cdot \mathbf{k}], \quad (45)$$

in which we are only interested in the magnitude of the velocity.

Along the same line of reasoning, in order to capture the anisotropy, the RT of the non-polar scattering by optical phonons can now be rewritten as

$$(\tau_{npol})_t(n, k) = \frac{\beta_t^2 \rho a_t^2}{\pi \hbar k_B T} \frac{1}{k_t^2} \left| \frac{\partial \epsilon_{n, k}}{\partial k_t} \right|. \quad (46)$$

The evaluation of the anisotropic ODP from *ab initio* methods is more involving than the evaluation of the ADP, since it characterizes the energy change of the carrier due to a relative atomic displacement. Therefore, external stresses that deform the unit cell as a whole cannot reveal ODPs, which have to be evaluated empirically on the basis of experimental data. The anisotropic RT of polar mode scattering of optical phonons can also be written as

$$(\tau_{pol})_t(n, k) = \frac{K_{pol} F_{pol} \zeta_t \hbar}{2e^2 k_B T} \left| \frac{\partial \epsilon_{n, k}}{\partial k_t} \right|, \quad (47)$$

with the anisotropic screening function given by

$$F_{pol} = \left[1 - \frac{1}{2(r_{0,t} k_t)^2} \ln[1 + 4(r_{0,t} k_t)^2] + \frac{1}{(1 + 4(r_{0,t} k_t)^2)} \right]^{-1}, \quad (48)$$

in which $r_{0,t}$ is the anisotropic screening radius defined from Eq.(29) as

$$r_{0,t}^{-2}(n, k) = \frac{4\pi e^2}{\zeta_{0,t}} \int -\frac{\partial f_0(\epsilon, \mu_t, T)}{\partial \epsilon_{n, k}} g(\epsilon) d\epsilon, \quad (49)$$

where it has been included the dependence on the band index n . The equilibrium electron distribution function, $f^{(0)}(\epsilon, \mu_t, T)$, is also defined to be anisotropic through an anisotropic electronic chemical potential μ_t , which will be discussed in detail below. In practice, the evaluation of density of states, $g(\epsilon)$, is obtained numerically on an energy grid with spacing $d\epsilon$ sampled over N_k \mathbf{k} -points

$$g(\epsilon) = \int \sum_n \delta(\epsilon - \epsilon_{n, \mathbf{k}}) \frac{d\mathbf{k}}{8\pi^3} = \frac{1}{\Omega N_k} \sum_{n, \mathbf{k}} \frac{\delta(\epsilon - \epsilon_{n, \mathbf{k}})}{d\epsilon}. \quad (50)$$

Similarly, the expression for the RT of scattering by ionized impurities has to be rewritten to include anisotropy as

$$(\tau_{imp})_t(n, k) = \frac{\hbar \zeta_{0,t}^2}{2\pi e^4 N_{i,t} F_{imp}(n, k_t)} k_t^2 \left| \left(\frac{\partial \epsilon_{n, k}}{\partial k_t} \right) \right|, \quad (51)$$

where the screening function has to be rewritten as $F_{imp}(n, k_t) = \ln(1 + \eta) - \eta/(1 + \eta)$, with $\eta = (2k_t r_{0,t})^2$, in which the anisotropic screening radius, $r_{0,t}$, has been defined by Eq.(49).

The electronic chemical potential, μ , is a result of the condition of charge neutrality. In principle, μ can be experimentally influenced mainly by doping, which determines the carrier concentration. The anisotropic electronic chemical potential, μ_t , as entering in the expressions for the RTs, $(\tau_{pol})_t$ and $(\tau_{imp})_t$, through their respective screening formulae, is a direct consequence of dissimilar carrier concentrations along different axial directions, as it has been measured by Zhao et al. [36] through Hall transport properties. It is important to stress that such measurements have been done along each axial direction separately and it does not mean three different chemical potentials simultaneously in a single system. The same line of reasoning has been adopted here by defining an anisotropic chemical potential, given that our calculations are performed independently for each axial direction. Given μ_t and T , the carrier concentration in the axis t can be calculated as the deviation from charge neutrality

$$n_{carr}(\mu_t, T) = Z - \int g(\epsilon) f^{(0)}(\epsilon; \mu_t; T) d\epsilon, \quad (52)$$

in which Z is the nuclear charge and $g(\epsilon)$ is the density of states as evaluated from Eq. (50). In practice, we can insert a target carrier concentration $n_{carr}^{(0)}$ within BoltzTraP, with $n_{carr}^{(0)} > 0$ ($n_{carr}^{(0)} < 0$) for holes (electrons) and μ_t is calculated iteratively up to $n_{carr}(\mu_t, T) \sim n_{carr}^{(0)}$ within a predefined criterium of 10^{-12} . The incremental variation of μ_t is given by

$$\Delta \mu_t = \frac{n_{carr}(\mu_t, T) - n_{carr}^{(0)}}{\int g(\epsilon) \frac{df^{(0)}}{d\epsilon} d\epsilon}, \quad (53)$$

and hence, a n -type semiconductor can be obtained if μ_t approaches the conduction band while a p -type material is obtained when μ_t moves to the valence band.

Once obtained the anisotropic RTs for each scattering process, the total anisotropic RT, $(\tau_{tot})_t$, that enters in the TE transport calculations can be derived from the Mathiessen's rule as

$$(\tau_{tot})_t^{-1}(n, k, \mu_t, T) = (\tau_{ac})_t^{-1}(n, k, T) + (\tau_{npol})_t^{-1}(n, k, T) + (\tau_{pol})_t^{-1}(n, k, \mu_t, T) + (\tau_{imp})_t^{-1}(n, k, \mu_t, T), \quad (54)$$

which is justified by considering the scattering mecha-

nisms as approximately independent. Once having $(\tau_{tot})_t$, the TDKs can be evaluated similarly to the calculation of the DOS as

$$\Xi_{tt}(\epsilon, \mu_t, T) = \frac{e^2}{\Omega N_k} \sum_{n, \mathbf{k}} (\tau_{tot})_t(n, \mathbf{k}, \mu_t, T) \mathbf{v}_{n, \mathbf{k}} \mathbf{v}_{n, \mathbf{k}}^T \frac{\delta(\epsilon - \epsilon_{n, \mathbf{k}})}{d\epsilon}, \quad (55)$$

where $\mathbf{v}_{n, \mathbf{k}}^T$ is the transpose of the vector $\mathbf{v}_{n, \mathbf{k}}$ given by Eq.(37) expanded over the band indices, and the matrix $\mathbf{v}_{n, \mathbf{k}} \mathbf{v}_{n, \mathbf{k}}^T$ is diagonal by construction. From the TDKs, the coefficient transport tensors, given by Eq.(12), can then be evaluated. For example, $\Lambda_{tt}^{(0)}(\mu_t, T) = \sigma_{tt}(\mu_t, T)$ is given by

$$\sigma_{tt}(\mu_t, T) = \int \Xi_{tt}(\epsilon, \mu_t, T) \left[\frac{-\partial f^{(0)}(\epsilon, \mu_t, T)}{\partial \epsilon} \right] d\epsilon, \quad (56)$$

which accounts for the diagonal terms of the electrical conductivity tensor. The diagonal terms of Seebeck coefficient tensor ($S_{tt}(\mu_t, T)$) is obtained by calculating $\Lambda_{tt}^{(1)}(\mu_t, T)$ as

$$\Lambda_{tt}^{(1)}(\mu_t, T) = \int \Xi_{tt}(\epsilon, \mu_t, T) (\epsilon - \mu_t) \left[\frac{-\partial f^{(0)}(\epsilon, \mu_t, T)}{\partial \epsilon} \right] d\epsilon, \quad (57)$$

in which $S_{tt}(\mu_t, T) = (eT)^{-1} \Lambda_{tt}^{(1)}(\mu_t, T) \cdot [\sigma_{tt}(\mu_t, T)]^{-1}$. Similarly, the diagonal terms of the corresponding coefficient tensor for the charge carrier contribution to the thermal conductivity, κ_{elec} , can also be determined. Its is important to note that, due to the factor $[-\partial f^{(0)}/\partial \epsilon]$, only bands within a few $k_B T$ from the Fermi level are relevant for transport properties.

IV. Results: The Case of Anisotropic SnSe

The methodology developed in the preceding sections was employed to investigate TE transport properties of p-type tin selenide (SnSe), which is one of the highest-performing TE materials available today. To perform the calculations, we have considered the RT models for scattering mechanisms introduced earlier. The polar scattering by acoustic phonons, known as piezoelectric scattering, has been neglected here. As emphasized by Li [62], for a typical III-V compound semiconductor, the piezoelectric scattering is usually much less important than the acoustic deformation potential scattering. The piezoelectric scattering becomes more important with increasing ionicity of the systems, for example, in most of the II-VI compound semiconductors, in which the wurtzite crystal structure lacks inversion symmetry, and, therefore, the piezoelectric stress tensor is nonvanishing.

On the basis of the facts above, it is expected that this kind of scattering mechanism is not relevant for IV-VI SnSe.

The choice to study SnSe is due to its following features. *i)* The charge carrier transport properties of SnSe have a strong anisotropy, which is expected due to its layered structure. *ii)* In particular, p-type SnSe presents strongly non-parabolic dispersion and its VBM has a *pudding-mold-like* shape [63]. *iii)* It is also noticed that the first and second VBMs can be considered degenerate, with an offset between them of only 0.02 - 0.06 eV [37]. *iv)* SnSe exhibits multiple local band edges aside from the global extrema, within an energy range comparable to the thermal energy of the carriers [64]. *v)* Moreover, SnSe has attracted much attention in recent years due to its record $zT \sim 2.6$ [36]. Therefore, based on the above features, we found SnSe to be a suitable material to test the methodology we are proposing here. Our results are compared with the experimental data provided by Zhao *et al.* [36, 37].

At room temperature, SnSe crystallizes in a layered orthorhombic structure with the $Pnma$ space group and 8 atoms in the unit cell. The nomenclature of the SnSe axes will follow that employed in the work of Zhao *et al.* Along the b - c plane, Sn and Se atoms are linked by strong covalent bonds ($\sim 2.80 \text{ \AA}$) forming a layered substructure with zig-zag chains along the b axis. The intralayer bonds are much stronger than the interlayer interactions. The latter are predominantly weak van der Waals-like Se-Sn bonds ($\sim 3.50 \text{ \AA}$) along the a -axis. Upon heating, SnSe undergoes a second-order phase transition to the higher symmetry $Cmcm$ phase around $T \sim 807 \text{ K}$, due to the condensation of the TO soft phonon mode of A_g symmetry at the BZ center (Γ). However, in this work, we are considering only the low-temperature $Pnma$ phase of SnSe, and, therefore, from now on, unless otherwise explicitly stated, SnSe will be referred only to this phase, without reference to the high-temperature phase.

A. DFT Calculation of Crystalline Structure and Band Structure

For the optimization of the crystalline structure and band structure calculations, we employed DFT within the generalized gradient approximation (GGA) in the formulation of Perdew-Burke-Ernzerhof (PBE) [65], as implemented in the VASP package [66, 67]. To model the ion cores, projector augmented-wave (PAW) pseudopotentials [68] were used, considering as valence electrons those in the orbitals $4d$, $5s$, and $5p$ of Sn and those in the orbitals $4s$ and $4p$ of Se. The electronic wave functions were expanded in a plane-wave basis-set with a kinetic-energy cutoff of 800 eV. To sample the BZ, a $4 \times 11 \times 12$ Monkhorst-Pack \mathbf{k} -point mesh was used for the force on the ions calculations. Subsequently, to determine the transport properties, we used a finer \mathbf{k} -mesh

of $16 \times 40 \times 43$, which ensures the calculated transport coefficients to be converged. Within BoltzTraP the original \mathbf{k} -mesh is then interpolated onto a mesh five times as dense ($M/N_{KS} = 5$). We used experimental structure [69] as starting configuration and relaxed the lattice parameters and atomic positions until all atomic force components were smaller than $1 \text{ meV}/\text{\AA}$.

The weak interactions between layers along a direction were accurately captured by incorporating van der Waals (vdW) corrections to DFT, according to the D3 approach as provided by Grimme *et al.* [70]. We found that DFT-D3 performed reasonably in predicting both the lattice parameters and the internal atomic positions of SnSe. We found that $a = 11.564 \text{ \AA}$, $b = 4.542 \text{ \AA}$ and $c = 4.166 \text{ \AA}$, diverging by 0.52%, 1.98% and 0.24%, respectively, from experimental lattice structure parameters determined at 300K [69]. The spin-orbit coupling (SOC) has been neglected in our calculations. As shown by Wu *et al.* [38] the neglect SOC does not lead to noticeable effects on the band structures, which has been attributed to the low symmetry of SnSe that removes the degeneracy of the electronic states.

The optimization of TE properties by chemical doping has been widely adopted. Particularly for SnSe, hole-doping by p-type dopants such as Ag [71–73] and Na [73] have led to enhancement of zT over a broad temperature range in comparison with the intrinsic (undoped) material. Here, we have also considered transport properties of hole-doped SnSe. An important modification caused in SnSe due to doping is the downward shift of chemical potential that enters in the valence band, turning the crystal into a metal. However, we have considered that the valence band shape has not changed considerably in relation to the intrinsic case due to doping, the so-called rigid band approximation.

B. Calculation of SnSe TE Transport Properties

1. Carrier Concentration for Intrinsic and Extrinsic P-Type Cases

In order to calculate TE transport properties for p-type SnSe, firstly it is necessary to properly estimate the hole concentration. On the basis of experimental anisotropic SnSe Hall coefficients [36, 37], from which Hall concentration, n_{Hall} , can be inferred for each axis, it is possible to acquire hints concerning the evolution of hole concentration with temperature. In particular, for intrinsic SnSe, Hall concentration stays almost constant within the range of $\sim 300 - 550 \text{ K}$, corresponding to non-equilibrium concentration of charge carriers due to growth conditions. At higher temperatures comprising the transition region ($\sim 550 - 807 \text{ K}$), a marked Arrhenius-type enhancement has been observed that is mainly related to thermally activated formation of vacancies accompanied by the production of holes [41]. The formation energies of intrinsic defects in SnSe has been

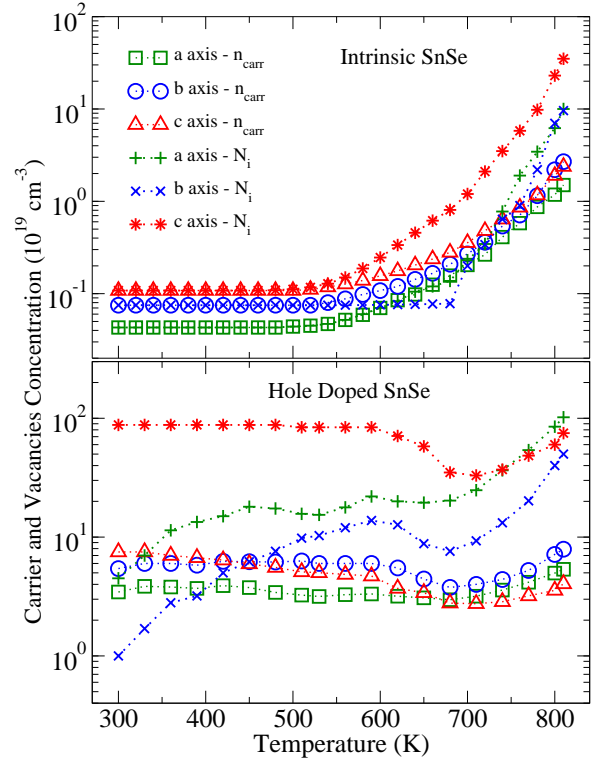


Figure 1: Evolution of carrier (n_{carr}) and vacancies (N_i) concentrations with temperature (300-810 K) in intrinsic SnSe (top panel) and in hole-doped SnSe (bottom panel) for each crystallographic axis.

systematically investigated on the basis of DFT [41, 74]. The Sn vacancy, V_{Sn} , exhibited the lowest formation energy with an ultra-shallow thermodynamic transition level. Hence, V_{Sn} plays a prominent role for p-type conduction in the absence of extrinsic doping. For example, depending upon the chemical potential, the Sn vacancy can be singly, $V_{Sn}^{(1-)}$, or doubly, $V_{Sn}^{(2-)}$, charged, by capturing one or two electrons and producing one or two holes for each created vacancy [41].

As pointed out by Kutorasinski *et al* [63], Hall concentrations should not be considered the actual hole concentrations because it is based on the assumption of a single parabolic band model and Hall scattering factor of unity. Hence, these measurements yield only an indication of the charge carrier concentrations. Despite of this qualitative aspect, the evolution of the experimental Hall coefficients suggests that the carrier concentration increases with temperature. Here, in order to determine the hole concentration, n_{carr} , we applied the condition that experimental Seebeck coefficients (S_{exp}) [36, 37] should be essentially the same as theoretical ones ($S_{theor}(\mu, T)$), that is, $S_{exp} = S_{theor}(\mu, T)$ for any temperature. This fitting is possible by varying the target hole concentration in the calculation of the Seebeck coefficients in Eq.(57). This is done through the neutrality condition (Eq.(52)); for a given concentration $n_{carr}(\mu_t, T)$ a corresponding chemi-

cal potential, μ_t , for each axis, is obtained. As n_{Hall} suggests that n_{carr} should be almost constant in the range of $\sim 300 - 550$ K, we kept constant n_{carr} in this range, which best adjust the experimental data. The resulting hole concentration, n_{carr} , is shown in the top panel of Fig. 1.

The same methodology has been applied for the case of hole-doped SnSe, in which the resulting hole concentration is shown in the bottom panel of Fig. 1. In this case, the evolution of hole concentration is much more involved and includes complex processes, such as the compensation effects, possibly due to the formation of doubly charged Se vacancies, $V_{Se}^{(2+)}$ and antisite defects, $Se_{Sn}^{(2+)}$, which will annihilate the holes created by acceptor impurities, such as Na, and vacancies, or due to the change in the charge state of the impurities. In fact, the measured Hall coefficients for the b and c axes highlights the tendency of the hole concentration to decrease with temperature, especially around 600 K Hall coefficient abruptly raises [37], in close correspondence with our results. Furthermore, the same tendency was also observed in Na and Ag-doped p-type SnSe, an specific kind of hole-doped SnSe [75]. Unlike metals, in which the conductivity decreases almost inversely with temperature, the conductivity of hole-doped SnSe decreases with the temperature following an exponential-like decay, suggesting that the carrier concentration are diminishing, as shown in the lower panel Fig. 1. Withal, the chemical potential shifts up with temperature as indicated by Fig. 2. Eventually, at elevated temperatures, an activated (semiconducting) behavior sets in, leading n_{carr} to increase, mainly above 700 K.

In the intrinsic case, at low temperatures ($T \lesssim 550$ K), the concentration of ionized impurities, N_i , is due to crystal growth conditions corresponding to a non-equilibrium concentration of vacancies. In this temperature range N_i has been considered to be almost the same as n_{carr} , since according to previous calculations [41], in the range of chemical potential determined in our calculations, the Sn vacancy is predominantly singly negatively charged, $V_{Sn}^{(1-)}$. However, at a given higher temperature, the thermally activated process of vacancy formation becomes relevant and we have to take into account the variation of N_i with temperature. This is done in our calculations by adjusting our calculated electrical conductivity to experimental results. In other words, the optimal values of N_i presented in the top panel Fig. 1, are the result of this fitting procedure.

The concentrations of ionized impurities for the extrinsic hole-doped SnSe are shown in the bottom panel of Fig. 1. As it was mentioned before, in the extrinsic case there are different charged impurities at play and the overall behavior is complex. The concentrations for the crystalline axes are somewhat related to their chemical potentials. It is important to notice that as temperature rises and the chemical potential becomes positive (enters the gap), there is a dip in the concentration of ionized impurities, this reduction is possibly caused by a change

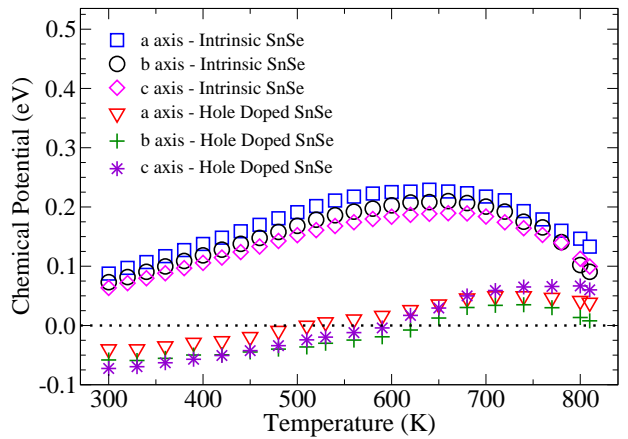


Figure 2: Evolution of the chemical potential with temperature (300-810 K) for both intrinsic and hole-doped SnSe for each crystallographic axis.

in the charge state of the impurities, which become neutral. Another interesting feature is that as temperature continues rising, the concentrations of ionized impurities increase steeply, possibly due to the creation of charged impurities, analogously to the intrinsic case, and the concentrations for each one of the axes seem to converge to a similar value.

2. SnSe Parameters for the RT Models

Once the temperature evolution of hole concentration is determined, it is possible to adjust RT models for TE transport modeling of SnSe. The parameters entering in the RT models for both cases of intrinsic and hole-doped SnSe are shown in Table I. In particular, ADP constants (E_1) have been extracted from DFT calculations by Guo *et al.* [76] for each axis. However, anisotropic renormalized effective ODP constants (β) have not been found in the literature, to the best of our knowledge. In this case, β values have been obtained by fitting our transport data for σ at 300 K to the experimental data [36]. Hence, the effective ODP's can be considered, as emphasized by Conwell [77], as effective couplings representing the actual coupling matrix elements that account for the more complex \mathbf{q} dependence. The resulting deformation potentials, both ADP and ODP constants, derived at 300 K, were directly applied throughout the full range of temperatures, extending up to ~ 810 K. It is also important to stress that deformation potential constants, were considered to be the same in both cases, intrinsic and hole-doped SnSe. The large anisotropy in the derived ODP constants is directly related to the strong and weak Sn-Se bonds in the crystal structure. It has been shown by heat capacity measurements the existence of two characteristic vibrational scales corresponding to hard and soft substructures [78].

As expected, DFT calculations with PBE functional

Table I: Parameters used to calculate the RTs of SnSe in the $Pnma$ phase. The parameters are ζ_0 (static dielectric constant)[79], ζ_∞ (high-frequency dielectric constant)[79], v_0 (sound velocity)[76], ρ (mass density), β (ratio of the average optical phonon energy and optical deformation potential constant), E_1 (acoustic deformation potential)[76], Gap energy[36] and K_{pol} (proportionality factor of Frölich interaction to account for the conduction of p-like symmetry holes).

Parameter	a axis	b axis	c axis
ζ_0	47	50	56
ζ_∞	18	15	15
v_0 (m/s)	3356	3267	3493
ρ (Kg/m ³)	6180	6180	6180
E_1 (eV)	14.1	15.8	16.4
β	0.000082	0.001702	0.000136
Gap (eV)	0.86	0.86	0.86
Lattice constant (Å)	11.564	4.542	4.166
K_{pol}	6.2	6.2	6.2

underestimate the band gaps. Consequently, for the purpose of comparison with experimental data, the calculations of the TE properties of SnSe were done by rigidly shifting upward the DFT-PBE conduction bands in order to attain the experimental value of the band gap 0.86 eV [36]. As will be discussed, the polar mode scattering by optical phonons dominate along b axis, consequently, we have adjusted the K_{pol} proportionality factor of the Frölich interaction to account for the conduction of p-like symmetry holes, which has been considered the same for all axes.

3. Main Scattering Mechanisms and RTs

Finally, a picture of the axial dependence of each scattering processes with temperature and chemical potential can be inferred from the average of each RT over the band indices n and the wavevectors \mathbf{k} ,

$$(\tau_x)_t(\mu_t, T) = \frac{1}{N_k \cdot N_{band}} \sum_n \sum_k (\tau_x)_t(n, k, \mu_t, T), \quad (58)$$

where N_k is the number of \mathbf{k} -points sampled, N_{band} is the number of bands, and x stands for the charge carrier scattering mechanism, namely, non-polar scattering by acoustic phonons (τ_{ac}), nonpolar scattering by optical phonons (τ_{npol}), polar scattering by optical phonons (τ_{pol}) and scattering by ionized impurities (τ_{imp}). The total average RT (τ_{tot}) is calculated through the Mathiessen's rule. The calculated average RTs as functions of the temperature for each axis of intrinsic and hole-doped SnSe are shown in Figs. 3 and 4, respectively. As it will be discussed below, in general, the dominant scattering mechanism varies with temperature and is not the same for each axis, highlighting the strong SnSe anisotropy.

The scattering by acoustic phonons strengthens with temperature, for both intrinsic and hole-doped SnSe, this

is intimately related to the enhancement in the number of available phonons for scattering as temperature increases. Figs. 3 and 4 show that the RT, τ_{ac} , associated with this process, decreases as $1/T$. In the b axis, the scattering by acoustic phonons plays a more prominent role than in the other axes, highlighting the strong anisotropy, however, this kind of scattering mechanism is only secondary in the overall transport process.

For the intrinsic case, the polar scattering by optical phonons strengthens as temperature increases, reducing τ_{pol} approximately as $1/T$ up to ~ 550 K. Above that temperature, this scattering process begins to weaken, consequently increasing τ_{pol} . This behavior is closely related to the onset of the thermally activated process of vacancies formation, which effectively increases the number of charge carriers in the material, hence inducing a stronger screening of the polarization. The onset of this screening effect on the polar scattering by optical phonons occurs in all axes at around the same temperature, however, this behavior mostly affects the overall transport in the a and b axes, in which τ_{tot} tends to increase following τ_{pol} , despite the competition with the other scattering processes.

The RT due to nonpolar scattering by optical phonons, τ_{npol} , also decreases as $1/T$, for both intrinsic and hole-doped SnSe. As discussed in the previous section, the strong anisotropy of SnSe is clearly shown by the fitted ODP constants $E_0 = \hbar\omega_0/\beta$. Even though, the ODP for the a axis is larger than that for the c axis, the resulting RTs is relatively smaller than that for the c axis, emphasizing the importance of the band velocities in the calculation of RTs.

The RT due to scattering by ionized impurities in the intrinsic case is almost constant up to temperatures at which the process of thermal creation of vacancies becomes relevant with respect to preexisting vacancies created during growth. Above those temperatures, the concentrations of vacancies begin to increase rather fast, and the RT associated with this scattering mechanism drops quite rapidly as well, for all three axes.

For hole-doped SnSe, the dominant scattering mechanisms are the nonpolar scattering by optical phonons and scattering by charged vacancies. The latter mechanism dominates along the b axis for the whole temperature range and becomes the primary scattering mechanism above 700 K for the a axis, while strongly affects the overall transport properties for the c axis at higher temperatures. It reflects the strong influence of the thermally activated process of vacancy formation for TE transport properties at higher temperatures, especially above 700 K. In fact, in the case of hole-doped SnSe, in which the holes concentration is large and the screening is stronger, the polar scattering by optical phonons practically does not cause pronounced effects on the transport properties, since $\tau_{pol} \sim 10^{-11}$ s.

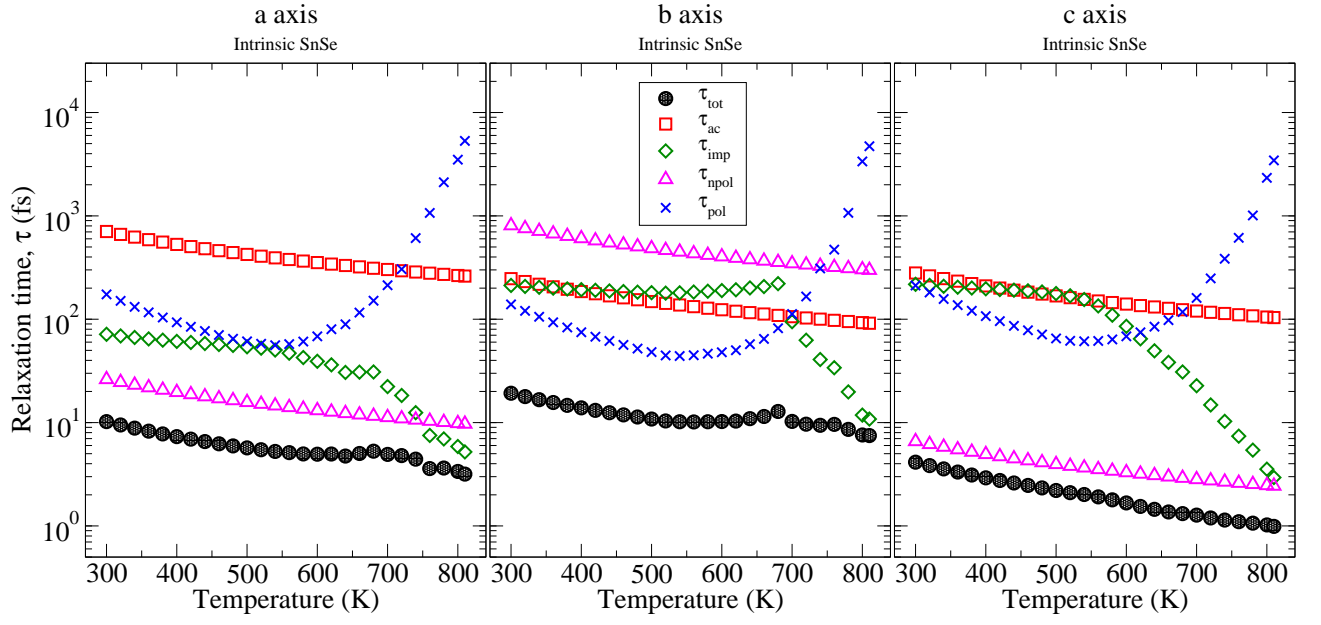


Figure 3: Temperature and axial dependence of average RTs calculated for each scattering process in intrinsic SnSe, namely, non-polar scattering of acoustic phonons (τ_{ac}), scattering by ionized impurities (τ_{imp}), non-polar scattering of optical phonons (τ_{npol}) and polar scattering of optical phonons (τ_{pol}). The average total RTs (τ_{tot}) that are calculated from the Mathiessen's rule are also shown as a function of temperature for each crystallographic axis.

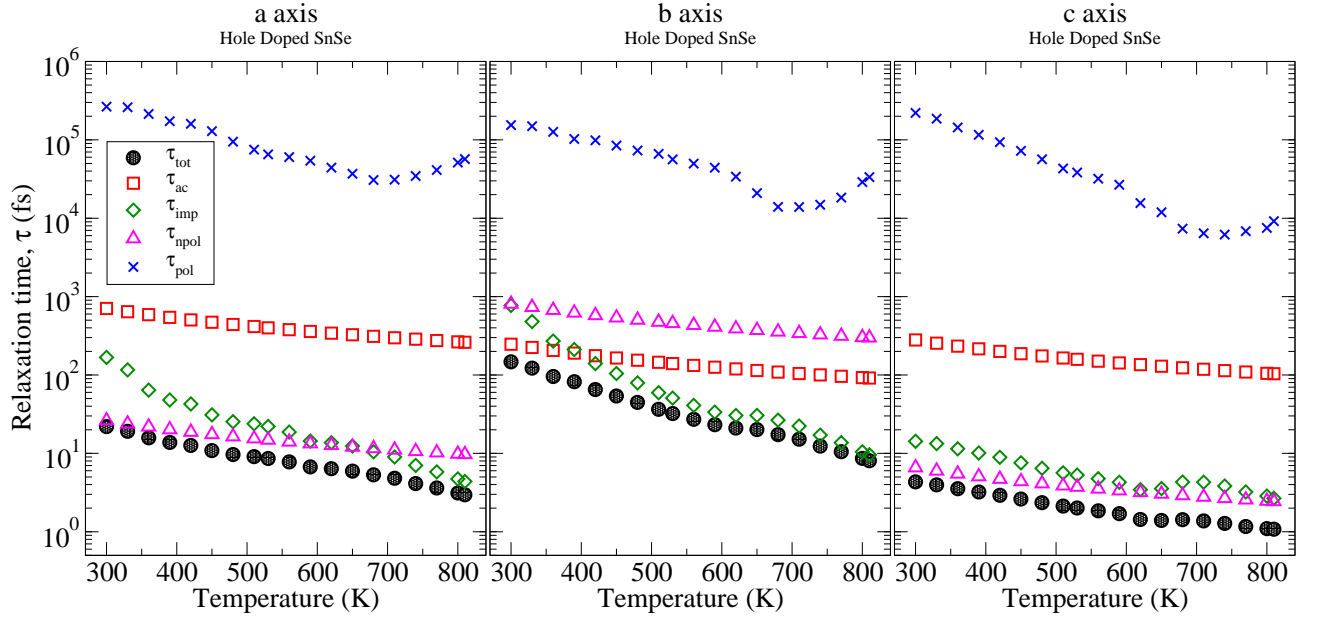


Figure 4: Temperature and axial dependence of average RTs calculated for each scattering process in hole-doped SnSe, namely, non-polar scattering of acoustic phonons (τ_{ac}), scattering by ionized impurities (τ_{imp}), non-polar scattering of optical phonons (τ_{npol}) and polar scattering of optical phonons (τ_{pol}). The average total RTs (τ_{tot}) that are calculated from the Mathiessen's rule are also shown as a function of temperature for each crystallographic axis.

4. Electrical Conductivity

Our results for the anisotropic electronic conductivity, σ , are in close agreement with experimental data [36, 37] (see Fig. 5). It is noteworthy to point out that, at first

glance, this good agreement would result solely from the fitting procedure used to obtain the concentration of ionized impurities, N_i , in the relaxation time τ_{imp} . This is not the case, because the electrical conductivity also depends on the chemical potential and carrier concentra-

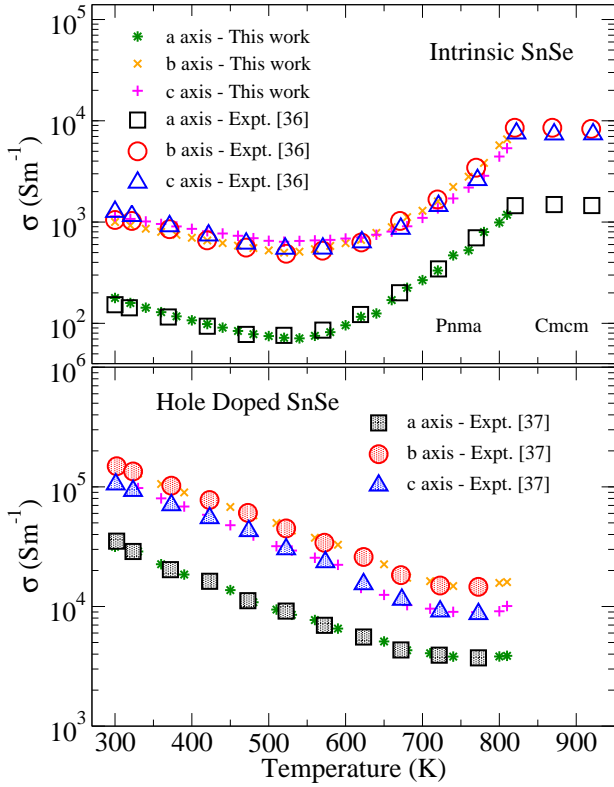


Figure 5: SnSe anisotropic electronic conductivity, σ , as a function of temperature, for intrinsic SnSe (top panel) and for hole-doped SnSe (bottom panel). Our findings are plotted along with experimental results [36, 37].

tion, which are obtained from the fitting of the calculated Seebeck coefficient to its experimental data. This indicates a consistency between the calculated Seebeck coefficient and electrical conductivity. The magnitude of σ along the a axis is almost one decade smaller than that for b and c axes. This is related to the strong anisotropy of the chemical bonding.

For intrinsic SnSe, between 300 – 550 K, σ decreases with temperature as a direct consequence of the enhancement of the scattering processes with temperature, while the hole concentration is maintained approximately constant in that temperature range. Above ~ 550 K, the thermally activated process of defects formation sets in and, consequently, σ markedly increases with temperature. This behavior is attained even though the scattering by charged vacancies becomes more relevant, however, the enhancement in the screening of the polar scattering by optical phonons largely compensates for the effect of scattering by ionized impurities. For the b axis the polar scattering by optical phonons dominates. Consequently, the overall scattering is strongly influenced by this mechanism. As the temperature increases and the activated process of vacancy formation sets in, the generation of more free carriers causes a stronger screening in this scattering mechanism, consequently increasing the electrical conductivity in the b axis to values even larger than those

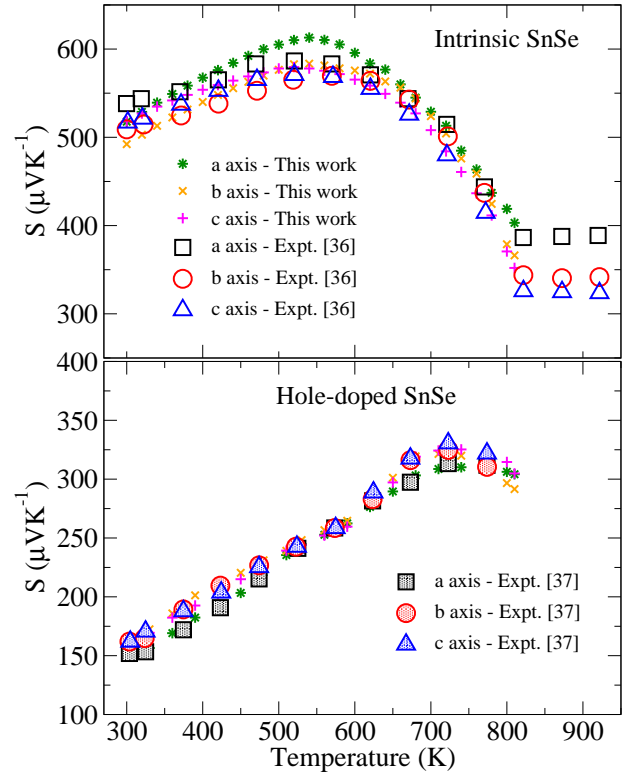


Figure 6: SnSe anisotropic Seebeck coefficient, S , as a function of temperature for intrinsic SnSe (top panel) and for hole-doped SnSe (bottom panel). Our findings are plotted along with experimental results [36, 37].

for the c axis for temperatures above ~ 550 K, where the mechanism of polar optical phonons scattering is only secondary.

In the case of hole-doped SnSe, σ presents a metal-like behavior, in which σ decreases steadily with temperature, up to high temperatures (~ 800 K), differently than what is observed in the intrinsic case. Above this temperature, σ tends to increase as a consequence of the pronounced enhancement in the hole concentration with temperature. In fact, this pronounced enhancement in the hole concentration begins around 670 K. However, unlike the intrinsic case, where σ begins to increase, for hole-doped SnSe, σ continues decreasing, highlighting the stronger influence of the scattering by ionized charged impurities.

5. Seebeck Coefficient

Our results for the Seebeck coefficients, S , as a function of temperature, are shown in Fig. 6 together with experimental results for both intrinsic SnSe [36] and hole doped SnSe [37]. The close agreement between calculations and experiment results from two facts: (1) the evolution of hole concentration with temperature was taken into consideration and (2) the relaxation times obtained from the electrical conductivity calculations are properly

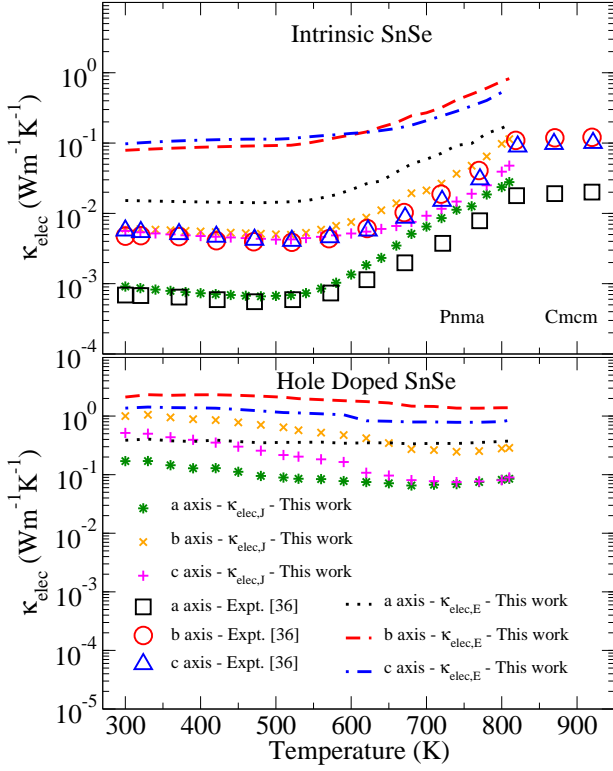


Figure 7: SnSe anisotropic thermal conductivities due to the carriers transport, $\kappa_{elec,J}$ and $\kappa_{elec,E}$, as functions of temperature for intrinsic SnSe (top panel) and for hole-doped SnSe (bottom panel). Our findings are plotted along with available experimental results for $\kappa_{elec,J}$ [36].

described. This demonstrates again the consistency between the calculated Seebeck coefficient and electrical conductivity. At ~ 550 K, the experimental Seebeck coefficients of intrinsic SnSe exhibit unpronounced maxima, which can be attributed mainly to the increase of hole concentration. A similar maximum occurs to the hole-doped SnSe, however at higher temperatures (~ 750 K).

6. Carrier Thermal Conductivity

Our results for the thermal conductivity due to the carrier transport are shown in Fig. 7, for both cases, intrinsic (top panel) and hole-doped (bottom panel) SnSe. These results are related to two dissimilar experimental situations, namely, $\kappa_{elec,J}$ and $\kappa_{elec,E}$. The former corresponds to the electric open-circuit condition where the electric current throughout the system is null. Experimentally, this situation corresponds to the measurement process performed by a device with high internal electrical resistance. The latter situation corresponds to the electric short-circuit condition where the electrochemical potential is constant throughout the system. Both experimental conditions are related by $\kappa_{elec,J} = \kappa_{elec,E} - T\sigma S^2$, resulting that $\kappa_{elec,E} > \kappa_{elec,J}$, as observed from Fig. 7.

Moreover, the thermal conductivity due to the carriers is greater in the hole-doped system compared to the intrinsic case.

The Lorenz number, L , defined as

$$L = \frac{\kappa_{elec,J}}{\sigma} T, \quad (59)$$

is commonly considered as a constant in order to determine $\kappa_{elec,J}$, a practice that is extensively used. Zhao *et al* [36] have considered the non-degenerate limit, where $L = 1.5 \times 10^{-8} \text{V}^2 \text{K}^{-2}$, to obtain $\kappa_{elec,J}$ for SnSe. Our findings for $\kappa_{elec,J}$ can be compared with Zhao's results for intrinsic SnSe in Fig. 7 (top panel). One can observe an excellent agreement for the three axis for temperatures $\lesssim 600$ K. It should be emphasized that our results for $\kappa_{elec,J}$ are completely free from any empirical fitting procedure. However, above ~ 600 K, for the a and b axes our results are greater than Zhao's results, which were determined considering L as a constant, while for the c axis our values are smaller than the experiment. Our results suggest the fact that L cannot be considered as a constant. Since SnSe has a complex band structure and the RTs have a complex behavior with the electron energy, L dependence on temperature and chemical potential should be taken into account. Such deviations between our results and Zhao's results may have significant implications, resulting in corrections to the earlier predicted values of the figure of merit [36], zT , which may have been overestimated for a and b axes and underestimated for c axis in the intrinsic case. Fig. 7 also depicts our results for $\kappa_{elec,E}$ for both cases intrinsic and hole-doped SnSe. It is important to note that in both cases $\kappa_{elec,E}$ is larger than $\kappa_{elec,J}$. The difference between these two thermal conductivities can be up one order of magnitude for the intrinsic case. This is a manifestation of the large power factor of SnSe.

Fig. 8 shows the results of our calculations for anisotropic L . At 300 K, L values are within the non-degenerate and degenerate limits, being the latter defined by the Wiedemann-Franz law [80]. As temperature increases, we can properly observe the variation of L for each crystallographic axis of both hole-doped and intrinsic SnSe. There is a large discrepancy between the results depending on the crystallographic axis. In general, L_c values for c axis tend to be around the non-degenerate limit or below, while for a and b axes the values are much larger. The ordering is basically $L_c < L_a < L_b$ at low temperatures, with an inversion between a and b axes as temperature increases. For the intrinsic case, above ~ 550 K, which is the onset temperature for vacancies formation, L_a begins to be greater than L_b . Similarly, such inversion occurs at a higher temperature, ~ 700 K, for the hole-doped case and can be attributed to a fast increase of $\kappa_{elec,J}$ for the a axis with temperature, which is not evident from Fig. 7 because of the logarithmic scale. At 810 K, L assumes very similar values for each one of the axes, for both cases hole-doped and intrinsic SnSe, because the carrier concentrations tend to be closer in

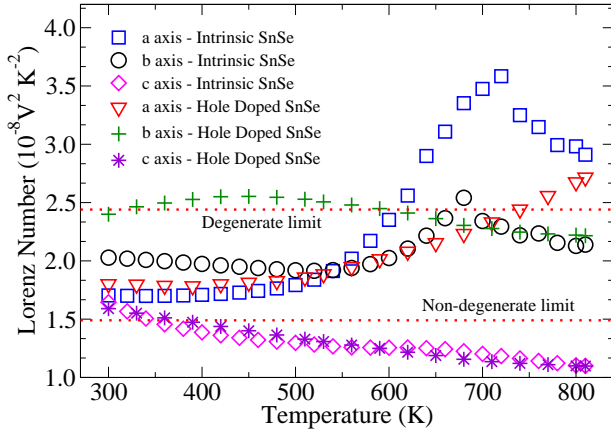


Figure 8: SnSe anisotropic Lorenz number, L , as a function of temperature for intrinsic SnSe and for hole-doped SnSe. The horizontal lines indicate the non-degenerate limit of semiconductors ($1.5 \times 10^{-8} \text{V}^2 \text{K}^{-2}$) and the degenerate limit ($2.44 \times 10^{-8} \text{V}^2 \text{K}^{-2}$) defined by the Wiedemann-Franz law.

both cases.

C. Summary

Based on the solution of the linearized BTE and using smooth Fourier interpolation of the KS eigenvalues and their corresponding velocities, we propose a methodology that incorporates models of anisotropic RTs for the main scattering mechanisms to calculate TE transport coefficients within the BoltzTraP code. The scattering mechanisms considered include the non-polar scattering by acoustic phonons (as described within the deformation potential theory), screened polar (based on the Frölich theory) and non-polar scattering (also within the deformation potential theory) by optical phonons and the scattering by ionized impurities with screening (within the Brooks-Herring approach). Such models for RTs include dependence on temperature, chemical potential and *ab initio* bandstructure, consequently, the methodology is able to directly capture important contributions to TE properties from multiple band edges, degenerate band edges and non-parabolicity effects on the same footing.

Therefore, our implementation allows to directly grasp and understand the physical mechanisms underlying the experimental data, including the knowledge of main scattering processes and their evolution with temperature and chemical potential. This methodology was applied to both intrinsic and hole-doped SnSe. For intrinsic SnSe, within the range 300–550 K, in which the hole concentra-

tion is approximately constant, σ decreases with temperature as a direct consequence of the enhancement of the scattering processes with temperature. Above ~ 550 K, the thermally activated process of defects formation sets in and, consequently, σ markedly increases with temperature, even though the scattering by charged vacancies becomes more relevant. However, the enhancement in the screening of the polar scattering by optical phonons largely compensates for the effect of scattering by ionized impurities. In the case of hole-doped SnSe, σ presents a metal-like behavior, with σ decreasing steadily as temperature increases, up to high temperatures (~ 800 K), highlighting the stronger influence of the scattering by ionized charged impurities.

Furthermore, toward transport properties optimization for TE applications, the methodology presented here can be extended to strained materials considering almost the same constants of unstrained systems. Particularly, this is a motivation for strained SnSe due to the sensitivity of its band-edge states to lattice strains [38]. Most importantly, the calculations take approximately the same amount of computational cost as the calculation using constant RT, as developed in the public version of BoltzTraP code. We expect that our approach can be applied to a broad range of semiconducting materials and potentially investigate the enhancement of TE properties in next-generation TE materials that explore materials anisotropy with multiplicity, degeneracy and non-parabolicity of the band edges.

Acknowledgements

ASC and AA gratefully acknowledge support from the Brazilian agencies CNPq and FAPESP under Grants #2010/16970-0, #2013/08293-7, #2015/26434-2, #2016/23891-6, #2017/26105-4, and #2019/26088-8. JJM acknowledges funding by the Ministerio de Economía y Competitividad, Agencia Estatal de Investigación, and Fondo Europeo de Desarrollo Regional (FEDER) (Spain and European Union) through Grant No. PGC2018-094763-B-I00, and by Junta de Extremadura (Spain) through Grant No. IB16013 (partially funded by FEDER). The calculations were performed at CCJDR-IFGW-UNICAMP in Brazil.

Computer Code Availability

All computer implementations of the methodology developed in this project were written in Fortran 90 and are available upon reasonable request.

[1] L. E. Bell, Science **321**, 1457 (2008).
 [2] M. G. Kanatzidis, Chemistry of Materials **22**, 648 (2009).

[3] L.-D. Zhao, S. Hao, S.-H. Lo, C.-I. Wu, X. Zhou, Y. Lee, H. Li, K. Biswas, T. P. Hogan, C. Uher, *et al.*, Journal

- of the American Chemical Society **135**, 7364 (2013).
- [4] S. Johnsen, J. He, J. Androulakis, V. P. Dravid, I. Todorov, D. Y. Chung, and M. G. Kanatzidis, *Journal of the American Chemical Society* **133**, 3460 (2011).
- [5] C. J. Vineis, A. Shakouri, A. Majumdar, and M. G. Kanatzidis, *Advanced Materials* **22**, 3970 (2010).
- [6] W. Liu, X. Tan, K. Yin, H. Liu, X. Tang, J. Shi, Q. Zhang, and C. Uher, *Physical Review Letters* **108**, 166601 (2012).
- [7] D. S. Parker, A. F. May, and D. J. Singh, *Physical Review Applied* **3**, 064003 (2015).
- [8] X. Chen, D. Parker, and D. J. Singh, *Scientific Reports* **3**, 3168 (2013).
- [9] D. Rode and S. Knight, *Phys. Rev. B* **3**, 2534 (1971).
- [10] J.-H. Bahk, Z. Bian, and A. Shakouri, *Phys. Rev. B* **89**, 075204 (2014).
- [11] P. Hohenberg and W. Kohn, *Physical Review* **136**, B864 (1964).
- [12] W. Kohn and L. J. Sham, *Physical Review* **140**, A1133 (1965).
- [13] L. Chaput, P. Pécheur, J. Tobola, and H. Scherrer, *Phys. Rev. B* **72**, 085126 (2005).
- [14] D. Hamann and D. Vanderbilt, *Phys. Rev. B* **79**, 045109 (2009).
- [15] W. E. Pickett, H. Krakauer, and P. B. Allen, *Phys. Rev. B* **38**, 2721 (1988).
- [16] K. Uehara and S. T. John, *Phys. Rev. B* **61**, 1639 (2000).
- [17] D. Koelling and J. Wood, *Journal of Computational Physics* **67**, 253 (1986).
- [18] G. K. Madsen and D. J. Singh, *Computer Physics Communications* **175**, 67 (2006).
- [19] D. J. Singh and M.-H. Du, *Physical Review Letters* **100**, 237003 (2008).
- [20] G. Hautier, A. Miglio, G. Ceder, G.-M. Rignanese, and X. Gonze, *Nature Communications* **4**, 2292 (2013).
- [21] A. F. May, D. J. Singh, and G. J. Snyder, *Phys. Rev. B* **79**, 153101 (2009).
- [22] D. Parker, X. Chen, and D. J. Singh, *Physical Review Letters* **110**, 146601 (2013).
- [23] J. He, M. Amsler, Y. Xia, S. S. Naghavi, V. I. Hegde, S. Hao, S. Goedecker, V. Ozoliņš, and C. Wolverton, *Physical Review Letters* **117**, 046602 (2016).
- [24] S. Poncé, W. Li, S. Reichardt, and F. Giustino, *Reports on Progress in Physics* **83**, 036501 (2020).
- [25] O. Restrepo, K. Varga, and S. Pantelides, *Applied Physics Letters* **94**, 212103 (2009).
- [26] B. Qiu, Z. Tian, A. Vallabhaneni, B. Liao, J. M. Mendoza, O. D. Restrepo, X. Ruan, and G. Chen, *EPL (Europhysics Letters)* **109**, 57006 (2015).
- [27] S. Poncé, E. R. Margine, and F. Giustino, *Physical Review B* **97**, 121201 (2018).
- [28] B. Himmetoglu, A. Janotti, H. Peelaers, A. Alkauskas, and C. G. Van de Walle, *Phys. Rev. B* **90**, 241204 (2014).
- [29] J.-J. Zhou and M. Bernardi, *Phys. Rev. B* **94**, 201201 (2016).
- [30] M. Rohlfling and S. G. Louie, *Phys. Rev. B* **62**, 4927 (2000).
- [31] C. Pellegrini, A. Marinelli, and S. Reiche, *Reviews of Modern Physics* **88**, 015006 (2016).
- [32] C. Bostedt, S. Boutet, D. M. Fritz, Z. Huang, H. J. Lee, H. T. Lemke, A. Robert, W. F. Schlotter, J. J. Turner, and G. J. Williams, *Reviews of Modern Physics* **88**, 015007 (2016).
- [33] R. M. Martin, *Electronic structure: basic theory and practical methods* (Cambridge university press, 2004).
- [34] F. Caruso, M. Troppenz, S. Rigamonti, and C. Draxl, *Phys. Rev. B* **99**, 081104 (2019).
- [35] S. Li, Z. Tong, and H. Bao, *Journal of Applied Physics* **126**, 025111 (2019).
- [36] L.-D. Zhao, S.-H. Lo, Y. Zhang, H. Sun, G. Tan, C. Uher, C. Wolverton, V. P. Dravid, and M. G. Kanatzidis, *Nature* **508**, 373 (2014).
- [37] L.-D. Zhao, G. Tan, S. Hao, J. He, Y. Pei, H. Chi, H. Wang, S. Gong, H. Xu, V. P. Dravid, *et al.*, *Science* **351**, 141 (2016).
- [38] Y. Wu, W. Xia, W. Gao, W. Ren, and P. Zhang, *Physical Review Applied* **8**, 034007 (2017).
- [39] J. M. Skelton, L. A. Burton, S. C. Parker, A. Walsh, C.-E. Kim, A. Soon, J. Buckeridge, A. A. Sokol, C. R. A. Catlow, A. Togo, *et al.*, *Physical Review Letters* **117**, 075502 (2016).
- [40] R. L. González-Romero, A. Antonelli, and J. J. Meléndez, *Physical Chemistry Chemical Physics* **19**, 12804 (2017).
- [41] A. Dewandre, O. Hellman, S. Bhattacharya, A. H. Romero, G. K. Madsen, and M. J. Verstraete, *Physical Review Letters* **117**, 276601 (2016).
- [42] B. M. Askerov and S. Figarova, *Thermodynamics, Gibbs Method and Statistical Physics of Electron Gases*, Vol. 57 (Springer Science & Business Media, 2009).
- [43] S. Ahmad and S. Mahanti, *Phys. Rev. B* **81**, 165203 (2010).
- [44] Y. I. Ravich, B. Efimova, and V. Tamarchenko, *Physica Status Solidi (B)* **43**, 11 (1971).
- [45] H. B. Callen, *Thermodynamics and an Introduction to Thermostatistics* (Wiley, 1985).
- [46] S. Hameau, Y. Guldner, O. Verzelen, R. Ferreira, G. Bastard, J. Zeman, A. Lemaitre, and J. Gérard, *Physical Review Letters* **83**, 4152 (1999).
- [47] J. Bardeen and W. Shockley, *Physical Review* **80**, 72 (1950).
- [48] C. Herring and E. Vogt, *Physical Review* **101**, 944 (1956).
- [49] H. Fröhlich, *Proc. Roy. Soc. (London)* **160**, 230 (1937).
- [50] H. B. Callen, *Physical Review* **76**, 1394 (1949).
- [51] D. Howarth and E. Sondheimer, *Proc. R. Soc. Lond. A* **219**, 53 (1953).
- [52] H. Fröhlich, *Advances in Physics* **3**, 325 (1954).
- [53] H. Ehrenreich, *Journal of Physics and Chemistry of Solids* **8**, 130 (1959).
- [54] D. Kranzer, *Physica Status Solidi (B)* **50** (1972).
- [55] M. Costato, C. Jacoboni, and L. Reggiani, *Physica Status Solidi (B)* **52**, 461 (1972).
- [56] D. Kranzer, *Journal of Physics C: Solid State Physics* **6**, 2977 (1973).
- [57] J. Wiley, *Phys. Rev. B* **4**, 2485 (1971).
- [58] H. Brooks, in *Advances in electronics and electron physics*, Vol. 7 (Elsevier, 1955) pp. 85–182.
- [59] D. Chattopadhyay and H. Queisser, *Reviews of Modern Physics* **53**, 745 (1981).
- [60] E. Moore, *Physical Review* **160**, 607 (1967).
- [61] D. G. Shankland, in *Computational Methods in Band Theory* (Springer, 1971) pp. 362–367.
- [62] S. S. Li, *Semiconductor physical electronics* (Springer Science & Business Media, 2012).
- [63] K. Kutorasinski, B. Wiendlocha, S. Kaprzyk, and J. Tobola, *Phys. Rev. B* **91**, 205201 (2015).
- [64] G. Shi and E. Kioupakis, *Journal of Applied Physics* **117**, 065103 (2015).

- [65] J. P. Perdew, K. Burke, and M. Ernzerhof, *Physical Review Letters* **77**, 3865 (1996).
- [66] G. Kresse and J. Hafner, *Phys. Rev. B* **48**, 13115 (1993).
- [67] G. Kresse and J. Furthmüller, *Phys. Rev. B* **54**, 11169 (1996).
- [68] G. Kresse and D. Joubert, *Phys. Rev. B* **59**, 1758 (1999).
- [69] K. Adouby, *Z. Kristallogr* **213**, 343 (1998).
- [70] S. Grimme, J. Antony, S. Ehrlich, and H. Krieg, *The Journal of Chemical Physics* **132**, 154104 (2010).
- [71] C.-L. Chen, H. Wang, Y.-Y. Chen, T. Day, and G. J. Snyder, *Journal of Materials Chemistry A* **2**, 11171 (2014).
- [72] H. Leng, M. Zhou, J. Zhao, Y. Han, and L. Li, *Journal of Electronic Materials* **45**, 527 (2016).
- [73] K. Peng, X. Lu, H. Zhan, S. Hui, X. Tang, G. Wang, J. Dai, C. Uher, G. Wang, and X. Zhou, *Energy & Environmental Science* **9**, 454 (2016).
- [74] Y. Huang, C. Wang, X. Chen, D. Zhou, J. Du, S. Wang, and L. Ning, *RSC Advances* **7**, 27612 (2017).
- [75] K. Peng, X. Lu, H. Zhan, S. Hui, X. Tang, G. Wang, J. Dai, C. Uher, G. Wang, and X. Zhou, *Energy Environ. Sci.* **9**, 454 (2016).
- [76] R. Guo, X. Wang, Y. Kuang, and B. Huang, *Phys. Rev. B* **92**, 115202 (2015).
- [77] E. M. Conwell, *High Field Transport in Semiconductors* (Academic Press, 1967).
- [78] S. R. Popuri, M. Pollet, R. Decourt, M. Viciu, and J.-W. G. Bos, *Applied Physics Letters* **110**, 253903 (2017).
- [79] H. Chandrasekhar, R. Humphreys, U. Zwick, and M. Cardona, *Physical Review B* **15**, 2177 (1977).
- [80] X. Wang, V. Askarpour, J. Maassen, and M. Lundstrom, *Journal of Applied Physics* **123**, 055104 (2018).